

Structural Refinement of the Tubulin Ligand (+)-Discodermolide to Attenuate Chemotherapy-Mediated Senescence[§]

Boying Guo, Alicia Rodriguez-Gabin, Andrea E. Prota, Tobias Mühlethaler, Nan Zhang, Kenny Ye, Michel O. Steinmetz, Susan Band Horwitz, Amos B. Smith, III, and Hayley M. McDaid

Department of Chemistry, Monell Chemical Senses Center and Laboratory for Research on the Structure of Matter, University of Pennsylvania, Philadelphia, Pennsylvania (B.G., N.Z., A.B.S.); Departments of Molecular Pharmacology (A.R.-G., S.B.H., H.M.M.), Epidemiology (K.Y.), and Medicine (H.M.M.), Albert Einstein College of Medicine, Bronx, New York; Laboratory of Biomolecular Research, Division of Biology and Chemistry, Paul Scherrer Institut, Villigen, Switzerland (A.E.P., T.M., M.O.S.); and University of Basel, Biozentrum, Basel, Switzerland (M.O.S.)

Received July 8, 2019; accepted May 13, 2020

ABSTRACT

The natural product (+)-discodermolide (DDM) is a microtubule stabilizing agent and potent inducer of senescence. We refined the structure of DDM and evaluated the activity of novel congeners in triple negative breast and ovarian cancers, malignancies that typically succumb to taxane resistance. Previous structure-activity analyses identified the lactone and diene as moieties conferring anticancer activity, thus identifying priorities for the structural refinement studies described herein. Congeners possessing the monodiene with a simplified lactone had superior anticancer efficacy relative to taxol, particularly in resistant models. Specifically, one of these congeners, B2, demonstrated 1) improved pharmacologic properties, specifically increased maximum response achievable and area under the curve, and decreased EC₅₀; 2) a uniform dose-response profile across genetically heterogeneous cancer cell lines relative to taxol or DDM; 3) reduced propensity for senescence induction relative to DDM; 4) superior long-term activity in cancer cells versus taxol or DDM; and 5) attenuation of metastatic characteristics in treated cancer cells. To contrast the binding of B2 versus

DDM in tubulin, X-ray crystallography studies revealed a shift in the position of the lactone ring associated with removal of the C2-methyl and C3-hydroxyl. Thus, B2 may be more adaptable to changes in the taxane site relative to DDM that could account for its favorable properties. In conclusion, we have identified a DDM congener with broad range anticancer efficacy that also has decreased risk of inducing chemotherapy-mediated senescence.

SIGNIFICANCE STATEMENT

Here, we describe the anticancer activity of novel congeners of the tubulin-polymerizing molecule (+)-discodermolide. A lead molecule is identified that exhibits an improved dose-response profile in taxane-sensitive and taxane-resistant cancer cell models, diminished risk of chemotherapy-mediated senescence, and suppression of tumor cell invasion endpoints. X-ray crystallography studies identify subtle changes in the pose of binding to β -tubulin that could account for the improved anticancer activity. These findings support continued preclinical development of discodermolide, particularly in the chemorefractory setting.

Introduction

(+)-Discodermolide (DDM; Fig. 1A) is a potent inducer of tubulin polymerization that has been evaluated as a chemotherapeutic in the taxane-refractory setting. However, despite its promise as anticancer molecule, DDM caused serious

interstitial pneumopathy in clinical evaluation (Mita et al., 2004), a condition typically associated with fibrosis and senescence (Jones, 2018). We previously characterized DDM as a potent inducer of chemotherapy-induced senescence (CIS) (Klein et al., 2005; Chao et al., 2011; Nadaradjane et al., 2018), defined as prolonged exit from proliferation that is distinct from quiescence.

It is widely accepted that anticancer therapies induce senescence to varying degrees (Ewald et al., 2010). CIS has been shown to be a causative factor in bleomycin-associated pulmonary toxicity (Aoshiba et al., 2013; Schafer et al., 2017) and doxorubicin-mediated cardiac toxicity and systemic inflammation (Demaria et al., 2017). Furthermore, toxicities from cancer therapy can prevent the completion of a prescribed

This work was supported by National Cancer Institute [Grant CA077263], the Breast Cancer Research Foundation, the National Foundation for Cancer Research, and the Swiss National Science Foundation [Grant 31003A_166608] (MOS). Research reported in this publication was also supported by the Albert Einstein Cancer Center Support Grant of the National Institutes of Health [Grant P30CA013330]. The content is solely the responsibility of the authors and does not necessarily represent the official views of the National Institutes of Health.

<https://doi.org/10.1124/mol.119.117457>.

[§] This article has supplemental material available at molpharm.aspetjournals.org.

ABBREVIATIONS: AUC, area under the curve; CIS, chemotherapy-induced senescence; DDM, discodermolide; E_{Max}, maximum response achievable; EMT, epithelial to mesenchymal transition; MTS, 3-(4,5-dimethylthiazol-2-yl)-5-(3-carboxymethoxyphenyl)-2-(4-sulfophenyl)-2H-tetrazolium; ROS, reactive oxygen species; SA- β -gal, senescence-associated β -galactosidase; SASP, senescence-associated secretory phenotype; SRB, sulforhodamine B; TNBC, triple-negative breast cancer.

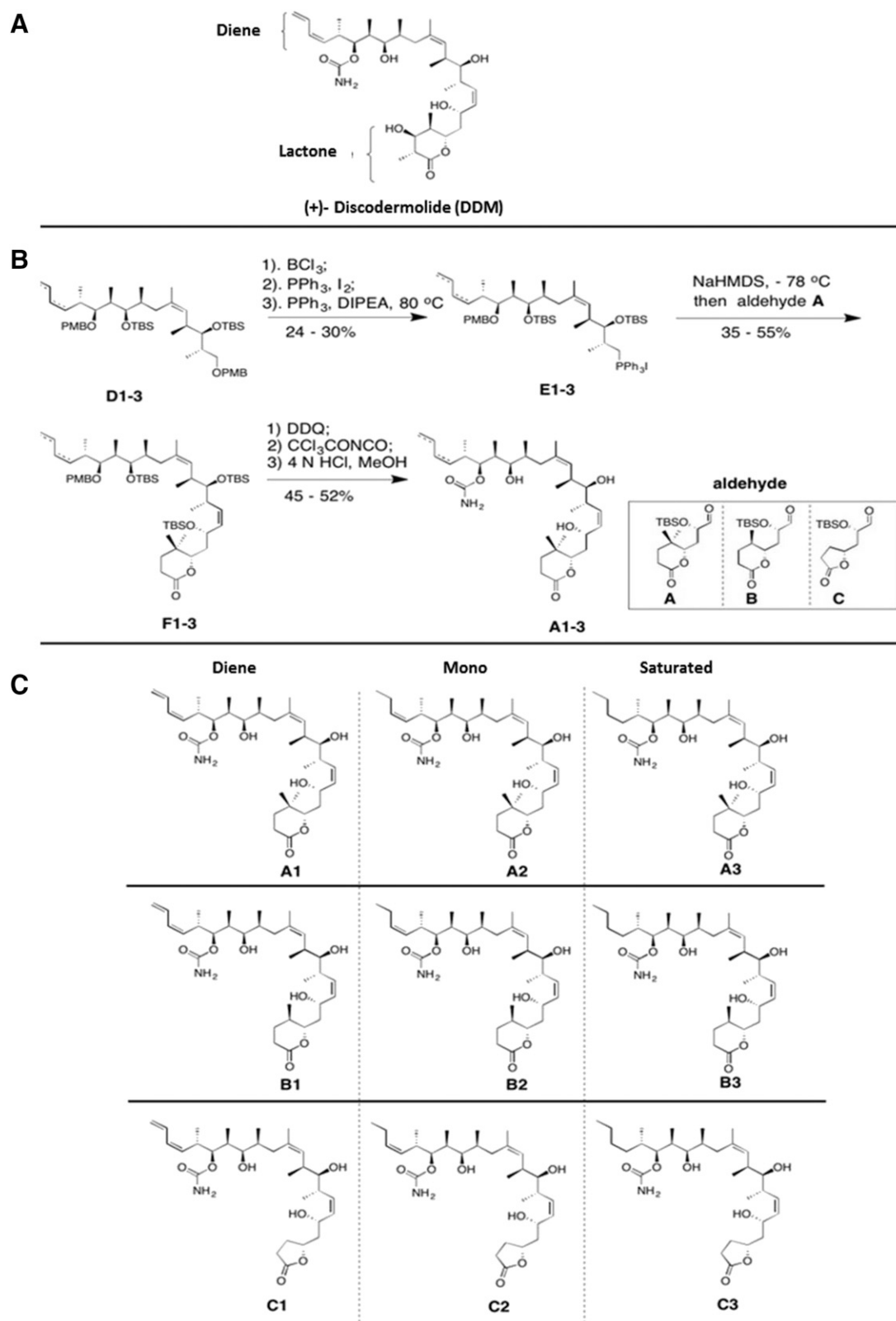


Fig. 1. Structure of (+)-DDM-modified congeners. (A) Chemical structure of (+)-DDM illustrating the lactone and diene moieties. (B) Representative synthesis of DDM analogs. (C) Structures of the congener series (A1–C3) available for biologic analysis.

course of treatment or thwart extended treatment. Aside from the collateral damage that CIS causes in nontransformed cells (Childs et al., 2015), tumor cells can also become senescent,

thereby evading the cell cycle-dependent action of many chemotherapeutic drugs (Samaraweera et al., 2012). These cells then become a source of chronic inflammation via the

senescence-associated secretory phenotype (SASP), which can accelerate disease progression via multiple effects on the tumor microenvironment (Laberge et al., 2012). Finally, senescent cancer cells can resume proliferation, giving rise to more tumorigenic progeny (Gosselin et al., 2009; Chao et al., 2011; Milanovic et al., 2018). Therapy-induced aneuploidization leading to replication stress and DNA damage signaling is a known driver of CIS (Santaguida et al., 2017; Watson and Elledge, 2017). Based on our experience with DDM both in vitro and in vivo, coupled with increased awareness that CIS can mediate the toxic effects of chemotherapy, we hypothesized that DDM-mediated senescence may have contributed to its toxicity in patients.

Taxol, unlike DDM, is a comparatively weak inducer of CIS (Klein et al., 2005; Nadaradjane et al., 2018). This is hypothesized to be due to variation in the affinity and pose of binding in the taxol-binding domain of tubulin (Prota et al., 2017), or binding of tubulin ligands to specific tubulin isoforms, or downstream effects thereof. Prior studies of DDM structure-activity relationships identified the lactone and diene moieties as regions for further modification that yielded congeners with superior anticancer activity (Smith et al., 2005, 2011; Smith and Freeze, 2007; Shaw, 2008). For example, C(1)-C(5) simplified lactone congeners were demonstrated to have superior anticancer activity in cancer cell lines (Shaw et al., 2005; Smith and Xian, 2005). Coincidentally, DDM is differentially metabolized by oxidation of C(4)-C(5) of the lactone and epoxidation of C(21)-C(22) or C(23)-C(24) diene (Fan et al., 2009). These observations led us to hypothesize that lactone and diene modifications could stabilize against oxidative metabolism and potentially influence anticancer activity. Building upon the original potential of DDM in the taxane-refractory setting, we set out to refine its chemical structure further.

We favored a multiparameter analysis approach (Fallahi-Sichani et al., 2013) to analyze the activity of these novel congeners. The most commonly used metric to describe pre-clinical activity is potency, or EC_{50} (the concentration at the half-maximal effect). However, potency typically describes doses associated with proliferative arrest rather than tumor cell death. Importantly, failure to consider other features of the dose-response relationship, such as maximum response achievable (E_{Max} ; efficacy), and area under the curve (AUC; potency and efficacy in a single measure) increases the probability of selecting molecules that are strong inducers of CIS. Thus, lead DDM congeners were identified on the basis of superior pharmacologic profiles (combined use of E_{Max} , AUC, and EC_{50}) relative to DDM or taxol, coupled with propensity to induce CIS, a cell fate that is largely ignored in drug development. Collectively, our data establish novel congeners of DDM as promising therapeutics for potential use in the chemorefractory setting.

Materials and Methods

Synthesis of Simplified DDM Congeners and X-Ray Crystallography Studies. DDM analogs were synthesized employing the Smith gram-scale synthetic route (Smith et al., 1999, 2000) with minor modifications. As shown in Fig. 1B, the primary para-methoxybenzyl ether in compounds D1–3 was selectively removed using 1.1 equivalents of BCl₃ in DCM at 0°C. The resulting primary alcohol was converted to the corresponding iodide that was used

without further purification in the next step due to the instability to provide the phosphonium salt E1–3. Treatment of the phosphonium salt E1–3 with sodium bis(trimethylsilyl) amide followed by the addition of the aldehyde fragment A led to the Wittig olefination products F. The para-methoxybenzyl protecting group was then removed using 1.2 equivalents of dichlorodicyanobenzoquinone followed by the introduction of the carbamate. Subsequent global deprotection of the tert-butyldimethylsilyl groups afforded DDM analogs A1–3. DDM analogs B1–3 and C1–3 were prepared in the same manner using aldehydes B and C. All compounds were dissolved in DMSO for cell-based analysis and diluted in culture media, such that the DMSO concentration was less than 0.01%. Methods for chemical synthesis and X-ray crystallography are provided in Supplemental Methods. Data collection and refinement statistics for T₂R-TTL-B2 are provided in Supplemental Table 6, and a simulated annealing electron density omit map highlighting the validity of the model is shown in Supplemental Fig. 5. The atomic coordinates and structure factors have been deposited in the Research Collaboratory for Structural Bioinformatics Protein Data Bank (www.rcsb.org) under accession number 6SES.

Cell Lines. Ovarian cancer, triple-negative breast cancer (TNBC), and lung cancer cell lines (SKOV3, IGROV1, HCC38, HCC1143, BT549, HS578T, HEY, A549, NIH-H460) and the BRCA mutant TNBC cell lines (HCC1937, MDA-MB-436) were purchased from American Type Culture Collection (Manassas, VA) and grown according to vendor recommendations. All cell lines were confirmed to be mycoplasma negative (Mycoplasma detection assay; Lonza) prior to use and early passages (<20) used. BRCA mutant SUM149PT cells were obtained from Dr. Steve Ethier, University of Michigan. All cell lines were authenticated by short tandem repeat profiling before purchase or use in this study. The resistant cell lines SKVLB and HeyTx100, derived from SKOV3 and HEY ovarian carcinoma cells, respectively, have been previously described (Bradley et al., 1989; Yang et al., 2018). Upon thawing they were grown in the presence of either vinblastine or taxol for two passages and subsequently cultured in drug-free media for a further two passages before use in experiments.

Cell Proliferation Assays. Standard cell proliferation assays were performed using both sulforhodamine B (SRB) to measure total protein in adherent cells (Skehan et al., 1990). Cells were seeded at $1-3 \times 10^4$ cells/ml into 96-well plates, and 24 hours later incubated with serial dilutions of congeners (2-fold), spanning nine dose levels, typically ranging from 250 to 1 nM ($n = 6$ wells per dose level). Cells were incubated for three doublings (3–7 days) without replenishing. The anticancer effect was computed relative to vehicle-only treated control cells, and sigmoidal dose-response curves were generated as described (Fallahi-Sichani et al., 2013). Resistant cell lines required a wide range of doses (1 μ M to 0.01 nM) to generate sigmoidal dose-response curves.

To assess the ability of congeners to suppress tumor cell proliferation in the long term, duplicate plates were also set up and analyzed approximately 3 weeks later, without replenishing media or congeners. In some cases, these data were reported as drug effect without normalization as control cells continued to proliferate over the duration of the experiment and eventually died, such that normalization could not be performed. SKOV3 cells are more taxol-sensitive relative to HEY; therefore, lower doses of all compounds were evaluated in this cell line.

For some experiments, the effect on congeners on cancer cell survival and proliferation was confirmed by a 3-(4,5-dimethylthiazol-2-yl)-5-(3-carboxymethoxyphenyl)-2-(4-sulfophenyl)-2H-tetrazolium (MTS) assay that measures NADPH/NADH production by dehydrogenase enzymes to reduce an MTS tetrazolium compound. The advantage of this method is that viability of both adherent and nonadherent cells can be determined (Segu et al. 1998).

Multiparameter Dose-Response Analysis. Data were analyzed as described previously (Fallahi-Sichani et al., 2013), whereby log-transformed values were fitted to a sigmoidal model using nonlinear least squares regression using the R statistical software suite

(<http://www.R-project.org/>). The features of interest, specifically EC_{50} , E_{Max} , AUC, and Hill slope, were computed in R from the fitted model. AUC was estimated using numerical integration (R function `integrate`) over the fitted model. The code is available upon request. E_{Max} (efficacy) is the maximum response achievable from a molecule. EC_{50} (potency) is the drug concentration corresponding to the half-maximal effect. AUC is a metric that represents the area under the relative viability curve, defined as the sum of measured responses, and combines potency and efficacy into one single parameter. Data were plotted in R and graphed as box and whisker plots depicting median (horizontal line) and interquartile range (boxes). Cancer cell lines with a Hill slope <1 and AUC <4.0 for taxol were categorized as taxol resistant (Supplemental Table 1) and analyzed as a separate cohort.

Statistics. With the exception of multiparameter dose-response analyses, all statistical analyses were performed using GraphPad Prism version 8 (GraphPad Software Inc.). Student's *t* tests were used to determine statistical significance of differences between the two groups. Where relevant, *P* values reported are from Dunnett's post hoc tests, adjusted for multiple variances. Equal variances analysis of E_{Max} and AUC between different congeners and taxol was done using a one-tailed F-test (Morgan, 1939). Differences were considered statistically significant at $P < 0.05$ with 0.01–0.001 being very significant and 0.001–0.0001 extremely significant.

Reactive Oxygen Species Generation. Reactive oxygen species (ROS) was measured in asynchronous and drug-treated HEY and A549 cells ($n = 6$) seeded in 96-well light-sensitive plates. Cells were treated with E_{Max} doses of taxol, DDM, or congeners (A1, A2, A3, B1, B2, and B3) for 3 hours prior to loading with 10 μ M H2DCFDA (a fluorogenic reagent that detects reactive oxygen intermediates in cells) in PBS for 40 minutes at 37°C in the dark to detect intracellular ROS (mean fluorescence intensity). Since congeners C had the weakest anticancer activity, they were not evaluated. H_2O_2 was used as a positive control. Fluorescence output was measured via plate reader (488 nm excitation/535 nm emission), and mean ROS production \pm S.D. was determined after subtraction of background fluorescence. There was no loss of cell viability within the 3-hour treatment period.

Determination of Senescence. Ninety-six-well plates of cells were set up as described for cell proliferation assays to determine senescence induction. After at least 6 days' treatment with various compounds (the minimal amount of time required to establish a stable senescent culture following exposure to cytotoxic compound), plates were processed for senescence-associated β -galactosidase (SA- β -gal) (Itahana et al., 2007). Positive cells were identified as having blue cytoplasmic staining coupled with an enlarged, granular cytoplasm using standard light microscopy at 10–20 \times magnification. Data were expressed relative to the number of SA- β -gal negative cells to differentiate between senescence and nonsenescent drug-tolerant cells that survive treatment. This assay was not informative for senescent SKOV3 cells.

Transwell Invasion Assay. Boyden Chamber assays were performed using BD Biocoat Matrigel Invasion Chambers. BT549 (metastatic TNBC) cells were seeded at 5×10^5 cells per chamber containing 0.5% serum. E_{Max} concentrations of test compounds were added, and invasion of cells through matrigel in response to a 0.5%–10% serum gradient was quantified 20 hours later by fixing membranes and staining invaded cells with crystal violet. Cells were counted by microscopy, excluding edges to determine the invasion rate (normalized to the effect of test compounds on cell viability by setting up identical plates without chamber inserts and quantifying the cell number 20 hours after treatment initiation). Data were expressed relative to vehicle-treated control, and experiments were repeated a minimum of three times.

Evaluation of Gene Expression in Cancer Cells Treated with Taxol or DDM Congeners. Total RNA was isolated from cells treated with various congeners using RNeasy, and cDNAs were synthesized using the Superscript VILO Reverse Transcriptase. Real-time quantitative reverse-transcription polymerase chain reaction

was performed using SYBRGreen I Master (Roche) and run on a LightCycler 480 (Roche) to determine expression of the epithelial to mesenchymal transition (EMT)-related genes, Twist, slug, snail, Vimentin, and CDH2. Expression was normalized to cyclophilin B and normalized to vehicle-treated controls. Experiments were performed in triplicate. Primers were designed using PrimerBank (<http://pga.mgh.harvard.edu/primerbank>).

Results

Synthesis of Simplified DDM Congeners. The main goal of this study was to refine the chemical structure of DDM, building on prior optimization studies focused on the lactone and diene regions (Fig. 1A). We hypothesized that monosaturation of the diene and addition of a methyl at C(4) of the lactone could limit oxidation and prevent metabolic degradation (Shaw et al., 2006), potentially modulating anticancer activity. Additionally, since conformationally rigid five-membered ring congeners demonstrated promising activity in previous studies (Shaw et al., 2005), diene-saturated variants of these were also synthesized (Fig. 1B), culminating in a series of congeners available for testing (Fig. 1C).

Multiparameter Analysis of Dose-Response Relationships Identifies Lead DDM Congeners. The anticancer activity of DDM congeners was determined in a panel of genetically heterogeneous human breast (TNBC) and ovarian cancer cell lines by multiparametric dose-response analyses, as described (Fallahi-Sichani et al., 2013). Median E_{Max} , AUC, and EC_{50} values were computed for all cell lines (Supplemental Table 1), and distribution was plotted (Fig. 2A). AUC and EC_{50} were statistically significantly different for DDM and taxol across all cell lines. Moreover, congeners A2 and B2 had the most significantly increased AUC ($P < 0.0001$) and EC_{50} ($P = 0.0002$ – 0.0001) relative to DDM (Supplemental Table 2). No significant differences in E_{Max} were evident for any of congener versus either taxol or DDM.

Dose-response plots for all data illustrate the variation in dose-response relationships for the four molecules, despite shared mechanism of action (Fig. 2B). DDM generated more linear shaped plots relative to the sigmoidal plots typical of taxol and congeners B2 and A2. Variances in the median AUC or E_{Max} of the congeners relative to taxol were evaluated using an F-test (Supplemental Table 3). The variation in median E_{Max} for B2 (but not A2) indicate some difference compared with taxol (F statistic, $P = 0.032$), with a trend toward significance for AUC also ($P = 0.070$), suggesting that B2 may generate a uniform pharmacologic response relative to taxol. However, this statistical significance may not hold after adjusting for multiple testing.

Definition of the Optimal C(21)-C(24) Terminus and Lactone Structural Elements of DDM. Epoxidation of the C(21)-C(22) or C(23)-C(24) diene was hypothesized to contribute to enzymatic degradation (Fan et al., 2009); therefore diene-monoene-saturated congeners were synthesized for evaluation. Saturated analogs (A3, B3, and C3) had weak anticancer activity irrespective of lactone, evident as high EC_{50} and low E_{Max} and AUC (Fig. 2B; Supplemental Table 1). Median E_{Max} for diene versus monoene congeners was comparable; however, monoenes (A2 and B2) had higher AUC and lower EC_{50} compared with dienes (A1 and B1) across all cell lines, though not statistically significant. Turning to the lactone, the addition of a second methyl group at the C(4)

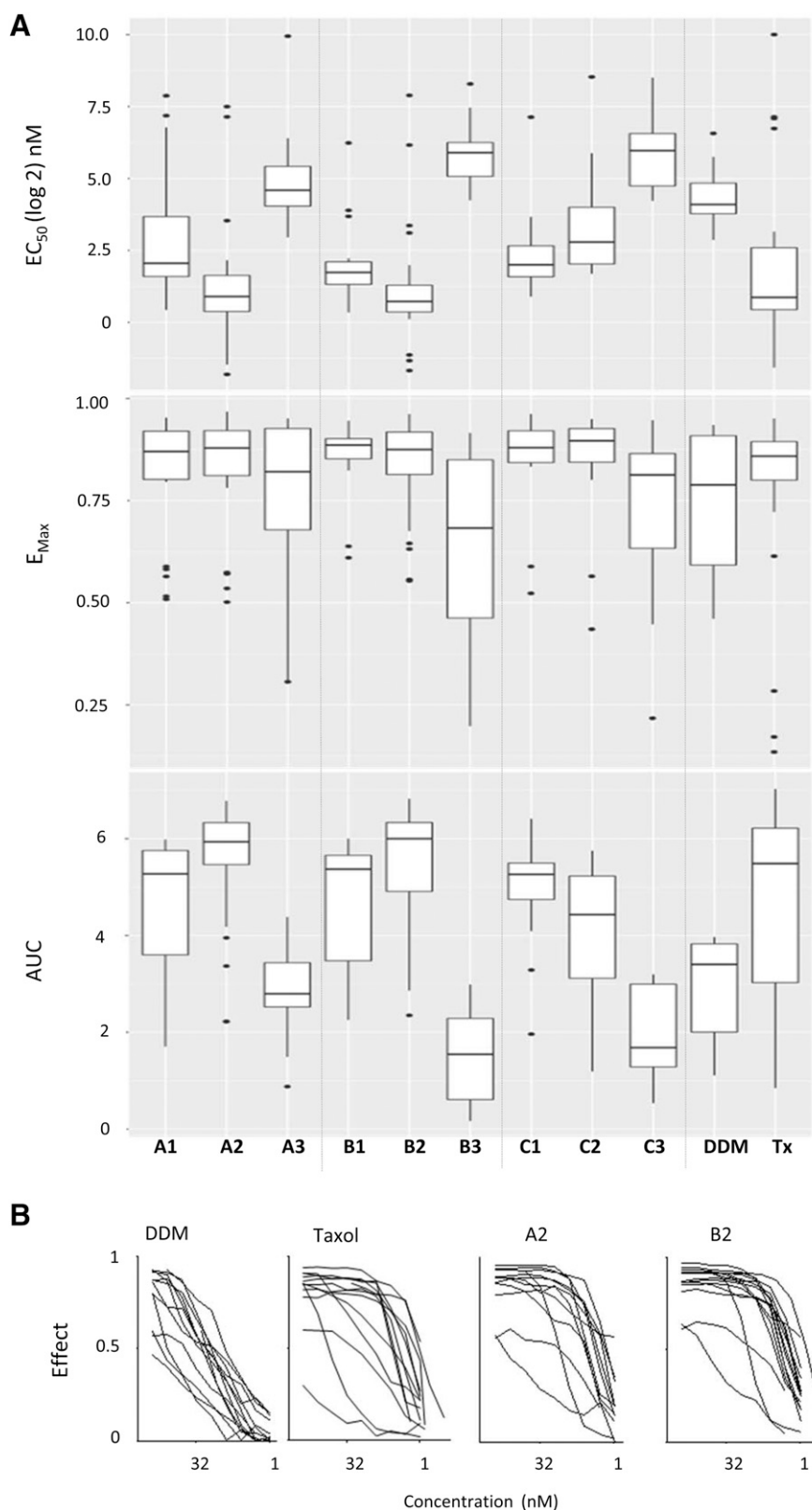


Fig. 2. Analysis of dose-response parameters for DDM, taxol, and novel DDM congeners across 12 TNBC and ovarian cancer cell lines identifies A2 and B2 as promising anticancer leads. (A) Variation in dose-response parameters for DDM, taxol (Tx), and congeners (A1–C3) across 12 TNBC and ovarian cancer cell lines. Values were computed from sigmoidal dose-response curves. Analysis parameters are EC_{50} (potency), E_{Max} (efficacy), and AUC (potency and efficacy combined). Data are represented as box and whisker plots with median (horizontal line) and interquartile range (boxes) shown. Bars extending to $1.5\times$ the interquartile range indicate variance for each parameter, and outliers are shown as nonconnected data points. (B) Dose-response curves depicting variation in dose-response relationships ($n = 12$, taxol: $n = 15$ for DDM, A2 and B2). Morgan testing indicates a statistically significant difference in the E_{Max} of B2 vs. taxol (F statistic, $P = 0.032$), although significance diminishes after adjustment for multiple testing.

position to form a gem dimethyl (congeners A1–A3) was designed to block oxidative metabolism of the C(4)–C(5) bond; however, there was only a subtle difference in dose-response parameters of these analogs relative to the B series that have one methyl at C(4) (Fig. 2B). In contrast, lactone congeners

with five-membered rings (series C) had weaker anticancer activity relative to both the A and B series. Within the C series, the diene-containing analog C1 was most active (Fig. 2A). Therefore, a DDM congener with a monoene and one C4-methyl is the optimal conformation for anticancer activity.

TABLE 1

ROS generation in DDM- and congener-treated cells Ovarian cancer cells (HEY) and NSCLC cells (A549) were treated with E_{Max} doses for 3 hours prior to loading with 10 μM 2',7'-dichlorodihydrofluorescein diacetate to detect intracellular ROS (measured as fluorescence intensity). Taxol induced ROS at levels comparable to H_2O_2 , whereas DDM induced ROS to a lesser extent. All congeners had statistically significantly reduced ROS activation compared with DDM in both cell lines (Dunnett's multiple comparison test). There was no statistically significant difference in ROS between congeners (e.g., A1 vs. A2) for either cell line (data not shown). Data represent means \pm S.D. of three independent experiments. H_2O_2 -treated cells were used as a positive control.

	HEY		A549	
	Fluorescence intensity \pm S.D.	<i>P</i>	Fluorescence intensity \pm S.D.	<i>P</i>
	χ		χ	
DDM	435 \pm 163.7	—	415 \pm 59.5	—
Taxol	1667 \pm 468.3	****	1546 \pm 522.8	ns
A1	173 \pm 22.0	****	145 \pm 11.1	**
A2	177 \pm 18.1	***	146 \pm 11.0	*
A3	172 \pm 44.7	**	148 \pm 6.6	*
B1	221 \pm 32.0	**	204 \pm 39.4	*
B2	199 \pm 21.1	****	170 \pm 16.2	**
B3	184 \pm 33.9	**	161 \pm 12.2	*
H_2O_2	1978 \pm 257.3	****	1703 \pm 116.0	*

* $P < 0.05$; ** $P < 0.01$ –0.001; *** $P < 0.001$ –0.0001; **** $P < 0.0001$; ns, not significant.

DDM Congeners Do Not Exhibit Significant Changes in Reactive Oxygen Species Generation.

Since DDM can be differentially oxidized at numerous sites including C(4)-C(5) and C(21)-C(22) or C(23)-C(24), we hypothesized that enzymatic hindrance at these sites could limit metabolic degradation. High ROS from mitochondrial oxidative damage in cells are associated with either senescence (Ziegler et al., 2015), cell death, or proliferation, depending on the cellular context (Olsen et al., 2013; Ogrunc et al., 2014). We hypothesized that metabolic degradation of DDM could generate high ROS, potentially causing senescence; therefore, we measured ROS generation as a surrogate for metabolic degradation. All congeners had reduced ROS relative to DDM within the parameters tested (Supplemental Fig. 1; Table 1). Levels were similar across A and B series suggesting that a simplified lactone structure and not the C4 constituent (methyl or gem-dimethyl) had the strongest influence on ROS generation. Similarly, there was no statistically significant difference in ROS levels that correlated with diene saturation. Taxol generated ROS at levels comparable to the positive control, H_2O_2 , and at statistically higher levels compared with DDM ($P < 0.05$); however, taxol is a weak inducer of senescence (Klein et al., 2005). Furthermore, comparing ROS generation with dose-response parameters (Fig. 2) and CIS (Fig. 4E), we conclude that ROS levels do not correlate with anticancer efficacy or CIS under the conditions evaluated here.

Identification of DDM Congeners with Activity in Taxol-Resistant Cell Models. To facilitate a nuanced dose-response relationship analysis, we dichotomized data into taxol-resistant versus taxol-sensitive cohorts. Resistant cell lines were identified as having AUC < 4 and Hill slope < 1 (Supplemental Table 4), consistent with previously described features (Sampah et al., 2011; Fallahi-Sichani et al., 2013). Analysis of sensitive cell lines indicated similar median AUC and EC_{50} among congeners A2 and B2 versus taxol (Fig. 3). In contrast, taxol had a weak anticancer effect in resistant cell lines, whereas both A2 and B2 had statistically significantly improved AUC ($P = 0.017$ and $P = 0.0072$, respectively) (Supplemental Table 4). Similarly, A2 and B2 had significantly improved EC_{50} .

Congener B2 Has Superior Long-Term Efficacy Compared to Taxol. Reported values for EC_{50} and E_{Max} for a given

cell line often vary widely due to differences in assay type and failure to tailor assays to account for differences in doubling time (Hafner et al., 2016), though our experimental design accounted for this. Colony-forming assays can be used to monitor longer-term anticancer efficacy; however, low seeding densities can artificially inflate efficacy metrics (Hafner et al., 2016). To circumvent this, we extended the duration of standard proliferation assays from three cell doublings to approximately 3 weeks without congener replenishment to evaluate long-term anticancer effect.

As shown for the ovarian cancer cell line HEY, dose-response curves for taxol and B2 were overlapping after three cell doublings (Fig. 4A) indicating almost identical effect. However, by day 21 (Fig. 4B), the dose-response curve for taxol was more shallow with substantially reduced AUC due to regrowth of transiently growth-arrested cells. Impressively, B2-treated cells sustained a strong anticancer response evident by day 21. Images of SRB-stained plates are shown at days 3 and 21 (Fig. 4, C and D). Measurement of mitochondrial oxidoreductase activity in both adherent and nonadherent drug-treated cells (MTS) also confirmed these findings (Supplemental Fig. 2). Since multiparameter analysis also indicated promising activity of congener A2, we contrasted the long-term effect of A2 versus B2 (Supplemental Fig. 2, C and D) and found that both had superior long-term activity compared with taxol; however B2 had the most sustained effect. As a control, the long-term activity of cisplatin (US Food and Drug Administration–approved therapy for serous ovarian cancer) was determined and found to have weak anticancer effect in HEY cells (Supplemental Fig. 2E). In conclusion, congener B2 displayed superior short- and long-term activity relative to taxol, cisplatin, and other DDM congeners. The effect of B2 was also evaluated in SKOV3 ovarian cancer cells (Supplemental Fig. 3), where short- and long-term analysis (4 days and 3 weeks) again indicated superior activity of B2 compared with taxol.

Attenuation of CIS by Congener B2. Since CIS is a major outcome of DDM exposure (Klein et al., 2005; Chao et al., 2011), we evaluated the lead congener, B2, for senescence inducing properties. HEY cells are amenable to senescence quantitation using the SA- β -gal assay (Itahana et al., 2007); therefore, four

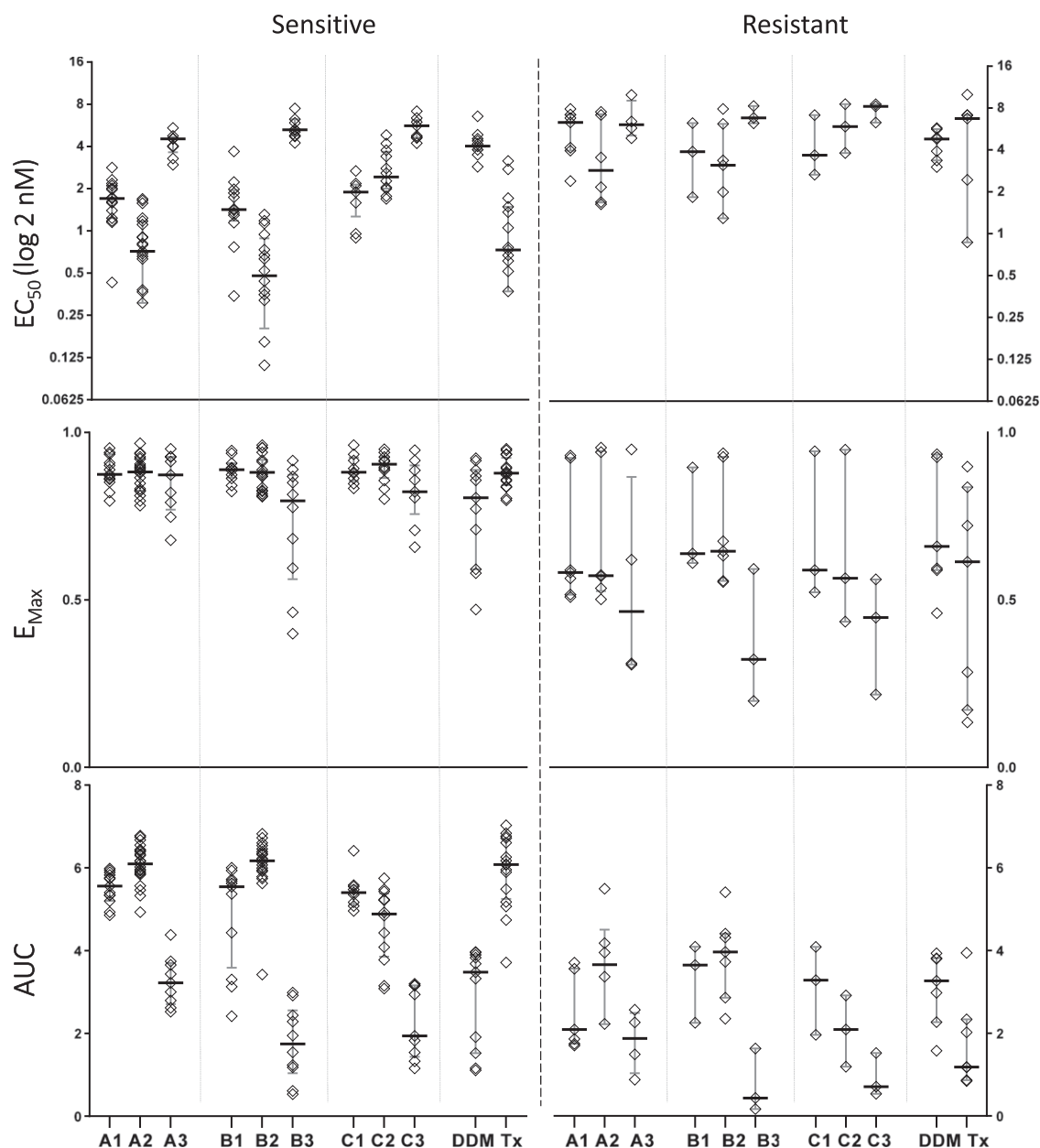


Fig. 3. Congeners with simplified lactones and monoenes have superior activity relative to DDM in chemorefractory cancer cell models. Values computed from sigmoidal dose-response curves for 12 cancer cell lines were segregated according to whether cells were dichotomized as taxol sensitive ($n = 9$) or taxol resistant ($n = 3$). Dose response parameters are represented as aligned dot plots indicating median (horizontal line) and interquartile range. Bars extending to $1.5\times$ the interquartile range are also indicated. Outliers are represented by nonconnected data points.

dose levels, approximating to E_{Max} , EC_{50} , and $>EC_{50}$, were evaluated for SA- β -gal positivity (Supplemental Table 5). As shown in Fig. 4E, DDM strongly induced senescence at 50 nM, a dose that approximated the 6-day EC_{50} . In contrast, taxol was a weak inducer of senescence, consistent with previous reports (Klein et al., 2005). Congener B2 had significantly reduced senescence relative to DDM at 50 nM ($P < 0.01$: analysis of variance with post hoc test), although the phenotype was still detected at a lower dose (Supplemental Table 5). Thus, at doses approximating the EC_{50} , congener B2 had attenuated risk of CIS relative to DDM.

We recently demonstrated that taxol does not possess significant senolytic activity, defined as the ability to induce senescent cell death (Samaraweera et al., 2017). Cisplatin and

the histone deacetylase inhibitor panobinostat, however, have strong senolytic activity. Thus, we evaluated the ability of DDM and congeners B2 and A2 to kill senescent HEY or A549 cells and found that like taxol, they possess little to no senolytic activity (Supplemental Fig. 4).

Superior Antimetastatic Properties of Congener B2. Since cancer mortality is primarily due to metastatic dissemination, we investigated the effect of congener B2, taxol, and DDM on metastatic parameters in BT549 (Fig. 5), an invasive, mesenchymal TNBC cell line (Lehmann et al., 2011). Images of congener-treated cells are shown to illustrate differential effects on morphology and proportion of surviving cells. The effect of the various tubulin ligands on EMT-associated genes in surviving, adherent cells was also evaluated. Expression of

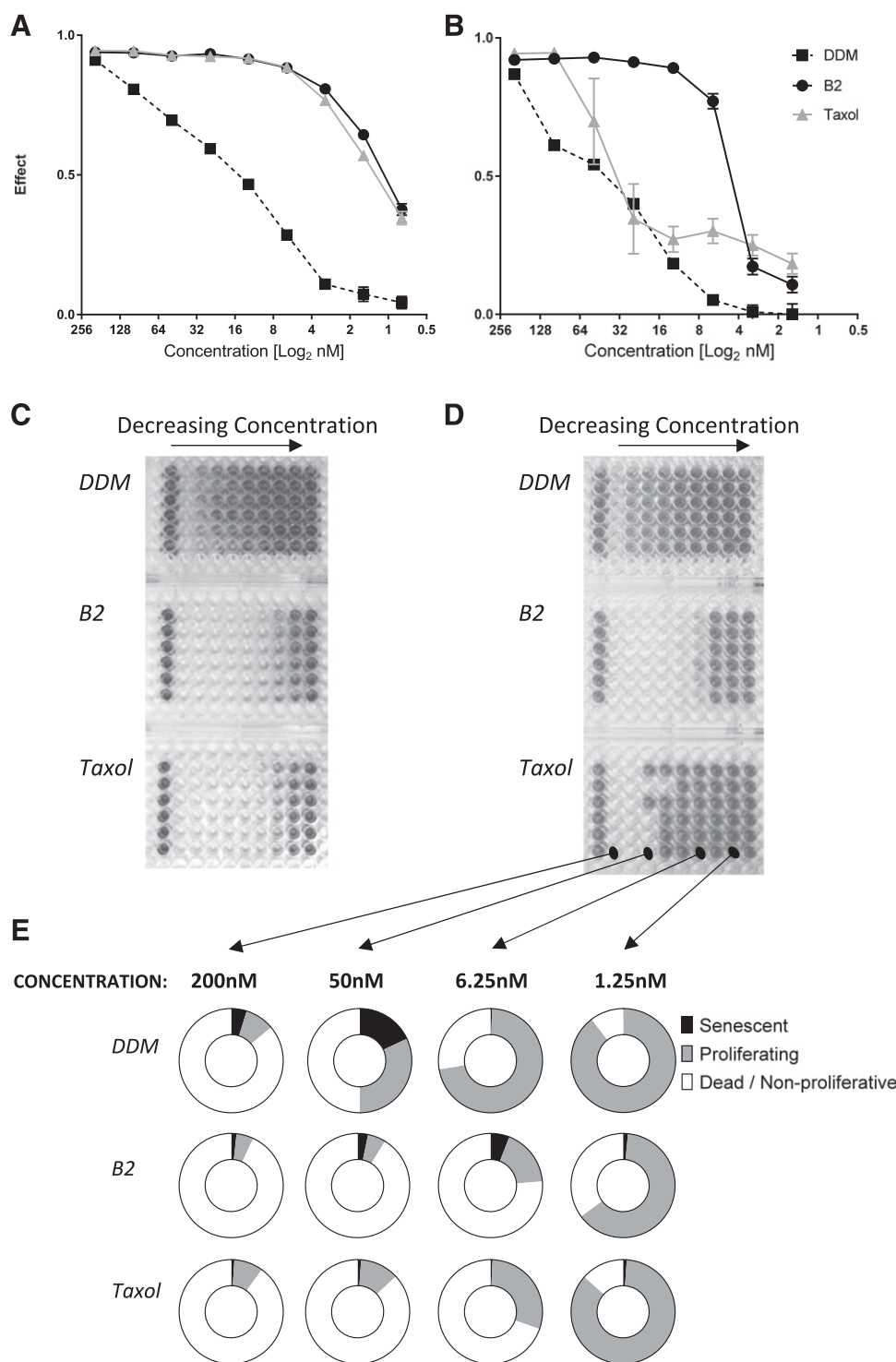


Fig. 4. Superior long-term efficacy of congener B2 in HEY cells. Dose-response curves for DDM, B2, and taxol in HEY cells after three cell doublings (3 days) (A) and 21 days without replenishing compounds or media (B). Representative images of SRB-stained plates corresponding to 3 days (C) and 21 days (D) are shown. (E) Quantitation of cell fate in drug-treated HEY cells after 6 days of treatment with DDM, B2, or taxol. Data were derived by quantifying percentage of SA- β -gal+ cells, a metric of senescence, as a proportion of drug effect. DDM strongly induced senescence relative to taxol, whereas B2 induced senescence at an intermediate rate. B2 demonstrated a prolonged anticancer effect, evident 3 weeks after dosing.

the transcription factors *snail* and *slug*, known regulators of EMT (Nieto et al., 1994; Batlle et al., 2000), was increased by taxol and DDM treatment, whereas B2-treated cells exhibited a statistically significantly decreased expression of all five genes comprising the EMT signature, relative to vehicle-only control ($P > 0.0001$: unpaired t test). The effect of taxol, DDM, or B2 on BT549 invasion through matrigel was also evaluated (Fig. 5C). All three suppressed invasion relative to vehicle-only controls; however, the effect was most pronounced for DDM and B2, though not statistically significant. Thus, congener

B2 treatment imparts favorable antimetastatic properties in this aggressive model of mesenchymal TNBC.

Congener B2 Binds to the Taxane Site with a Shifted Lactone Compared with DDM. The binding mode of DDM in the taxane pocket of β -tubulin has recently been described in great detail by X-ray crystallography (Prota et al., 2017). To provide critical insights into the molecular mechanism of action of the lead congener, B2, we determined the crystal structure of a tubulin-B2 complex to 2.0 Å resolution (Fig. 6). B2 bound to the taxane site on β -tubulin in a very similar

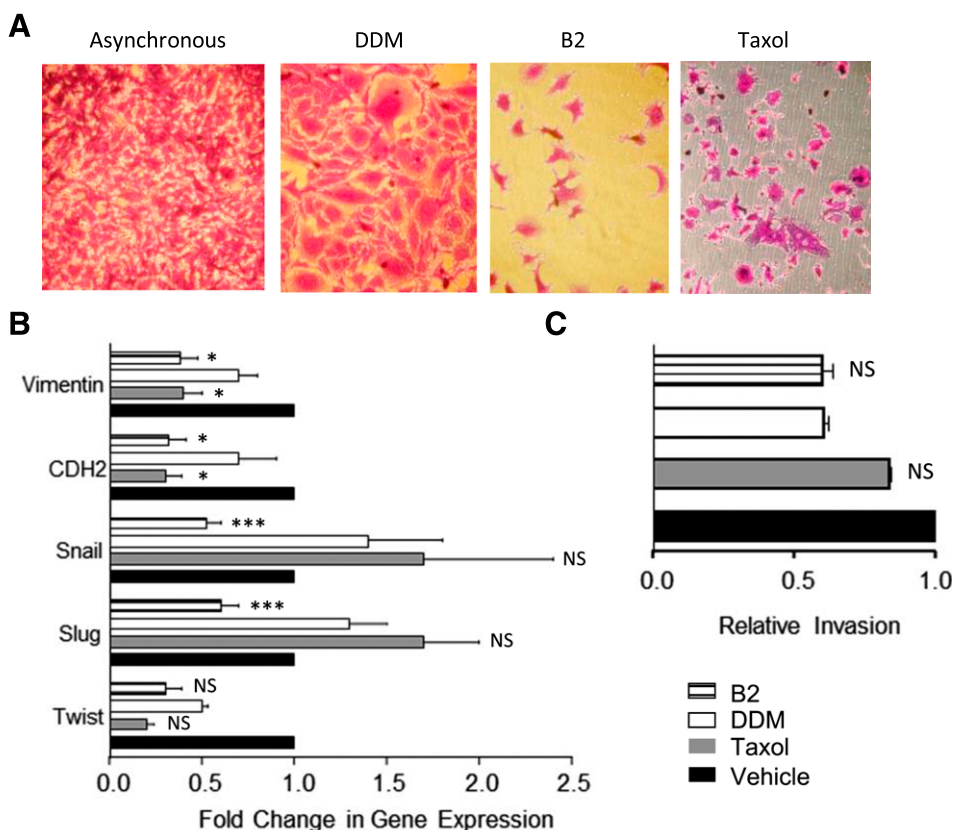


Fig. 5. Antimetastatic activity of B2 in chemorefractory TNBC cells. BT549 cells were exposed to either EC_{50} doses of DDM, B2, or taxol for 4 days (A, B) or E_{Max} doses for 24 hours (C) and subsequently assayed for metastasis-related endpoints. (A) SRB-stained cells show enlarged, flat cells emerging after DDM treatment, consistent with emergence of a senescent phenotype. In contrast, B2- and taxol-treated cells have reduced numbers of surviving cells that do not have the same morphology. (B) Analysis of a five-gene metastatic signature following the various treatments indicates a statistically significant decrease in expression relative to the effect of either taxol or DDM. Statistical significance for B2 and taxol compared with DDM is indicated. (C) 24-hour treatment of BT549 with taxol, DDM, or B2 partially suppresses invasion through matrigel. Statistical significance relative to DDM (unpaired *t* test) is indicated. Data represent means \pm S.D. of three independent experiments. **P* < 0.05; ****P* < 0.001–0.0001; NS, not significant.

hairpin conformation as DDM (Fig. 6A), and the majority of the interactions were conserved. However, compared with DDM, the absence of both the C2-methyl and the C3-hydroxyl in B2 gave rise to a loss of one hydrogen bond to the backbone of Arg369 and a reorientation of the lactone ring in the pocket (Fig. 6B). Moreover, a smaller reorientation of the C23 and C24 section of the monoene sidechain was observed, which caused a minor shift of the Arg278 sidechain. These observations demonstrate that B2 binds to the taxane site on β -tubulin. They further suggest a better adaptation capability to changes in the taxane-binding site of congener B2 compared with DDM.

We further superimposed the taxol-bound MT structure (Fig. 6C, Protein Data Bank identifier 5SYF) onto the taxane site of the tubulin-B2 complex (root mean square deviation of 0.99 Å over 49 C_{α} -atoms). Compared with taxol, B2 and DDM occupied the structural cavities previously reported (Prota et al., 2017) by positioning their lactone rings between the C4-acetyl and the 3'-phenyl moieties, relative to taxol. There were also significant differences in the orientation of Arg 278 by DDM and B2 versus taxol, which are potentially significant for future molecular dynamic studies, since amino acids Ser 277 and Arg 278 are variant among human tubulin isotypes. Overall, these data provide structural insights in support of a favorable occupation of B2 in the binding pocket of tubulin that associate with improved biologic activity relative to DDM.

Discussion

Cytotoxic chemotherapies cause an array of fates in tumors, including apoptosis, necrosis, mitotic catastrophe, and the dormancy phenotypes, quiescence and senescence. CIS is an

unintended consequence of cancer treatment that imparts long-term consequences that may contribute to accelerated aging in cancer survivors and increased risk of developing a secondary malignancy, reviewed in Childs et al., 2015. Thus, minimizing risk of CIS is an important but underappreciated consideration in anticancer drug development. We have implemented a robust strategy to select molecules that maximize tumor cell death while minimizing CIS based on increasing E_{Max} and AUC and steepening the Hill slope (Fallahi-Sichani et al., 2013; Nadaradjane et al., 2018). This multiparametric approach best maximizes leads for further development, evolving contemporary drug discovery beyond an EC_{50} -centric approach and thereby lessening the risk of developing compounds that strongly induce CIS.

Although the tumor-suppressive effects of senescence prevents the replication of damaged cells that could potentially become malignant, this applies primarily to young cells and tissues (Baker et al., 2011; Braumüller et al., 2013; Storer et al., 2013; Flach et al., 2014; Katsimpardi et al., 2014). However, in cancer cells, the integrity of the cell cycle regulatory apparatus is compromised such that they can escape or bypass senescence, enabling malignant cell expansion (Damsky et al., 2015; Sharpless and Sherr, 2015; Le Duff et al., 2018). For this reason, prosenescent cancer therapies have largely fallen out of favor due to concerns regarding chronic SASP signaling and tumor evolution (Milanovic et al., 2018). A significant exception to this, however, is the approval of combined CDK4/6 inhibitors with antiestrogens for the treatment of estrogen receptor-positive, human epidermal growth factor receptor 2-negative breast cancer (Wolff, 2016). The mechanism of action is partially attributable to senescence induction in tumors that retain retinoblastoma function,

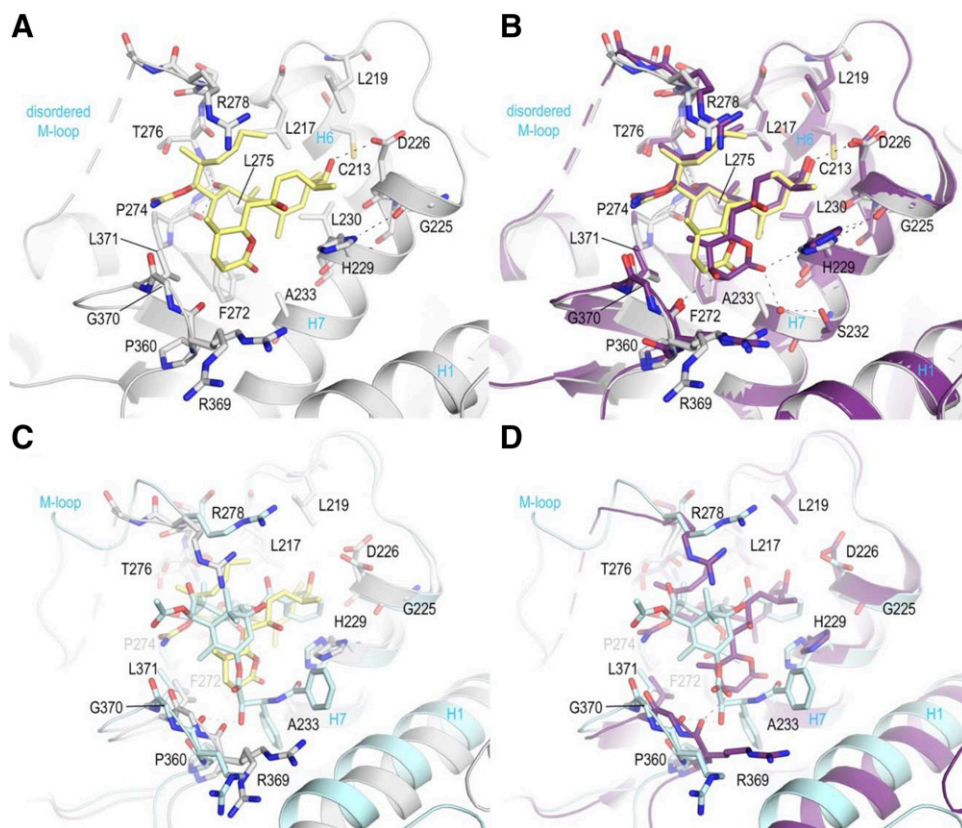


Fig. 6. Structure of the tubulin-B2 complex infers optimal adaptation in the taxane-binding pocket. (A) Close-up view of the interactions observed between congener B2 (yellow) and β -tubulin in white stick and ribbon representation. Hydrogen bonds are depicted as black dashed lines, water molecules as red spheres. (B, C) Close-up view of the superimposed tubulin-DDM (violet purple) (B) and paclitaxel-stabilized microtubule (pale cyan, Protein Data Bank identifier 5SYF) (C) complexes in stick and ribbon representation. (D) The complexes were superimposed onto their corresponding taxane-site residues 208–219, 225–237, 272–276, 287–296, 318–320, and 359–376 (root mean square deviation_{DDM} 0.12 [45 C $_{\alpha}$ -atoms]; root mean square deviation_{paclitaxel} 0.9 [49 C $_{\alpha}$ -atoms]).

with subsequent immune-mediated clearance in some patients (Knudsen and Witkiewicz, 2017). Thus, it is hypothesized that therapy-mediated senescence in tumors with intact G1/S checkpoint function and a low prevalence of genetic alterations can lead to favorable clinical outcome (Knudsen and Witkiewicz, 2017). However, the majority of solid malignancies approved for treatment with taxol, including breast and ovarian cancers, do not meet these criteria; therefore, drug effect is highly variable, as demonstrated by our dose-response modeling. In light of these considerations, it is significant that the lead DDM congener, B2, has a more uniform dose-response profile relative to taxol and DDM, despite the significant genetic variability of the cell lines tested.

We set out to define, synthesize, and test congeners for potent anticancer activity including diminished risk of CIS, a dominant mechanism of action of DDM (Klein et al., 2005). DDM-mediated senescence is durable, based on the time it takes for resistant clones to emerge (Chao et al., 2011); therefore, it is not surprising that congener B2 also induces senescence, albeit at significantly reduced levels relative to the parent molecule. Despite justifiable concerns about inducing senescence in solid tumors, retention of some CIS activity across a narrow dose range could impart favorable outcome, specifically in terms of longevity of the response, as demonstrated by the sustained effect of B2 after 3 weeks that was superior to taxol. Furthermore, trepidation related to sustained SASP signaling from persistent senescent cells could be allayed by our finding that cisplatin, typically administered sequentially after taxol, is a potent senolytic that can kill senescent cancer cells (Samaraweera et al., 2017).

We are interested in uncovering mechanistic insight at the level of the tubulin-ligand interaction to account for the

improved dose-response relationship of B2 relative to DDM or taxol. Clearly, modulation of the lactone and diene confer increased E_{Max} and AUC such that cell killing is a more prevalent mechanism of action for congeners A2 and B2. However, this may be due to mechanisms distal to tubulin polymerization, including enhanced cellular uptake and resistance to efflux and/or resistance to metabolic degradation. These attributes will be determined in future mouse studies to evaluate systemic toxicity and in vivo efficacy of these molecules.

Other explanations include mechanisms proximal to the tubulin-ligand interaction, including different binding affinity of B2 compared with DDM or taxol, thereby inducing differential effects on tubulin dimers and/or the microtubule lattice. To address this, we generated a crystal structure of the tubulin-B2 complex to uncover the molecular interaction and demonstrated a shift in the occupation of the lactone of B2 versus DDM in the taxane site. Minor changes were observed at the monoene moiety. Thus, removal of both the C2-methyl and C3-hydroxyl could render B2 more adaptable to changes in the taxane site and provide a molecular basis to account, at least partially, for the improved anticancer activity of B2 versus DDM.

Although the crystallography studies were done using bovine brain tubulin, we are cognizant of the fact that the tubulin family is composed of multiple isoforms, each assumed to possess functional specificity within a given cell type. It is plausible that DDM binds a specific tubulin isoform with a specialized function in G1/S checkpoint integrity or similar, such that perturbation causes potent senescence. Lactone and diene modifications could also influence binding to distinct tubulin isoforms that ultimately modulates cellular fate, i.e., death versus senescence. Although the lactone binding

domain of human tubulins is largely invariant, there are isotype-defining amino acid changes in the diene-interacting domain that could potentially modulate tubulin-ligand interactions. Delineating such interactions would prove invaluable in guiding future structural refinements of DDM. This requires biochemical testing that presently is challenging for studies of human tubulin, although additional studies are ongoing to address these questions and to provide critical insight into the molecular mechanism of action of B2, a promising anticancer molecule.

Acknowledgments

The authors acknowledge the assistance of Dr. Chia-Ping H. Yang in preparing congener stock solutions.

Authorship Contributions

Participated in research design: Guo, Prota, Steinmetz, Horwitz, Smith, McDaid.

Conducted experiments: Guo, Rodriguez-Gabin (cell-based analysis), Prota (X-ray crystallography), Mühlethaler (protein expression, purification and crystallization), Zhang (chemical synthesis).

Contributed reagents and analytic tools: Ye, Smith.

Performed data analysis: Rodriguez-Gabin, Prota, Ye (biostatistics), Steinmetz (structure analysis), McDaid (cell-based analysis).

Wrote or contributed to the writing of the manuscript: Guo, Rodriguez-Gabin, Prota, Mühlethaler, Zhang, Ye, Steinmetz, Horwitz, Smith, McDaid.

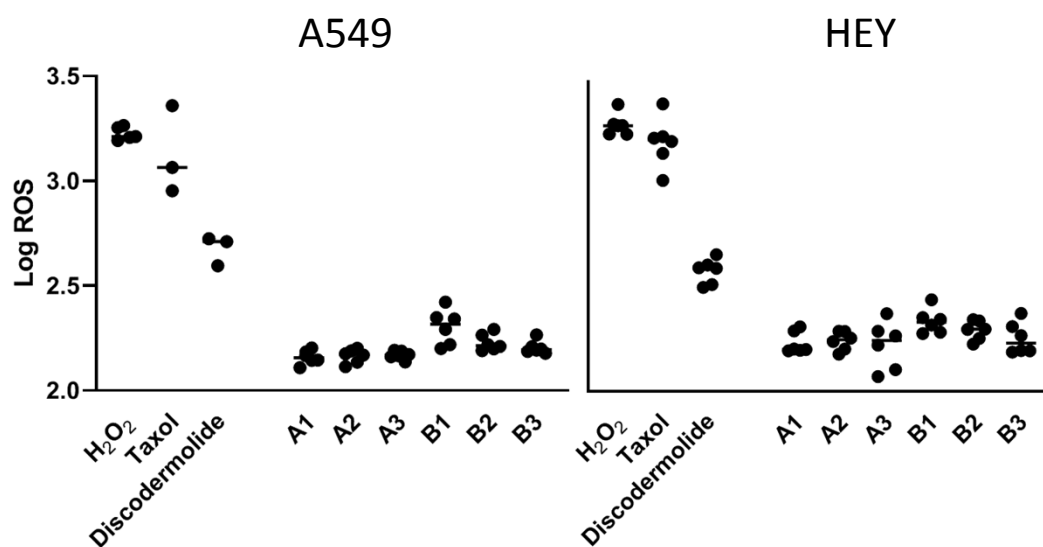
References

- Aoshiba K, Tsuji T, Kameyama S, Itoh M, Semba S, Yamaguchi K, and Nakamura H (2013) Senescence-associated secretory phenotype in a mouse model of bleomycin-induced lung injury. *Exp Toxicol Pathol* **65**:1053–1062.
- Baker DJ, Wijshak T, Tchoknia T, LeBrasseur NK, Childs BG, van de Sluis B, Kirkland JL, and van Deursen JM (2011) Clearance of p16Ink4a-positive senescent cells delays ageing-associated disorders. *Nature* **479**:232–236.
- Battle E, Sancho E, Franci C, Dominguez D, Monfar M, Baulida J, and García De Herreros A (2000) The transcription factor snail is a repressor of E-cadherin gene expression in epithelial tumour cells. *Nat Cell Biol* **2**:84–89.
- Bradley G, Naik M, and Ling V (1989) P-glycoprotein expression in multidrug-resistant human ovarian carcinoma cell lines. *Cancer Res* **49**:2790–2796.
- Braumüller H, Wieder T, Brenner E, Altmann S, Hahn M, Alkhaled M, Schilbach K, Essmann F, Kneilling M, Griessinger C, et al. (2013) T-helper-1-cell cytokines drive cancer into senescence. *Nature* **494**:361–365.
- Chao SK, Lin J, Brouwer-Visser J, Smith AB III, Horwitz SB, and McDaid HM (2011) Resistance to discodermolide, a microtubule-stabilizing agent and senescence inducer, is 4E-BP1-dependent. *Proc Natl Acad Sci USA* **108**:391–396.
- Childs BG, Durik M, Baker DJ, and van Deursen JM (2015) Cellular senescence in aging and age-related disease: from mechanisms to therapy. *Nat Med* **21**:1424–1435.
- Damsky W, Micevic G, Meeth K, Muthusamy V, Curley DP, Santhanakrishnan M, Erdelyi I, Platt JT, Huang L, Theodosakis N, et al. (2015) mTORC1 activation blocks Brav600E-induced growth arrest but is insufficient for melanoma formation. *Cancer Cell* **27**:41–56.
- Demaria M, O'Leary MN, Chang J, Shao L, Liu S, Alimirah F, Koenig K, Le C, Mitin N, Deal AM, et al. (2017) Cellular senescence promotes adverse effects of chemotherapy and cancer relapse. *Cancer Discov* **7**:165–176.
- Ewald JA, Desotelle JA, Wilding G, and Jarrard DF (2010) Therapy-induced senescence in cancer. *J Natl Cancer Inst* **102**:1536–1546.
- Fallahi-Sichani M, Honarnejad S, Heiser LM, Gray JW, and Sorger PK (2013) Metrics other than potency reveal systematic variation in responses to cancer drugs. *Nat Chem Biol* **9**:708–714.
- Fan Y, Schreiber EM, and Day BW (2009) Human liver microsomal metabolism of (+)-discodermolide. *J Nat Prod* **72**:1748–1754.
- Flach J, Bakker ST, Mohrin M, Conroy PC, Pietras EM, Reynaud D, Alvarez S, Diolaiti ME, Ugarte F, Forsberg EC, et al. (2014) Replication stress is a potent driver of functional decline in ageing haematopoietic stem cells. *Nature* **512**:198–202.
- Gosselin K, Martien S, Pourtier A, Vercamer C, Ostoich P, Morat L, Sabatier L, Duprez L, Tkint de Roodenbeke C, Gilson E, et al. (2009) Senescence-associated oxidative DNA damage promotes the generation of neoplastic cells. *Cancer Res* **69**:7917–7925.
- Hafner M, Niepel M, Chung M, and Sorger PK (2016) Growth rate inhibition metrics correct for confounders in measuring sensitivity to cancer drugs. *Nat Methods* **13**:521–527.
- Itahana K, Campisi J, and Dimri GP (2007) Methods to detect biomarkers of cellular senescence: the senescence-associated beta-galactosidase assay. *Methods Mol Biol* **371**:21–31.
- Jones KD (2018) Unclassifiable interstitial lung disease: a pathologist's perspective. *Eur Respir Rev* **27**:170132.
- Katsimpardi L, Litterman NK, Schein PA, Miller CM, Loffredo FS, Wojtkiewicz GR, Chen JW, Lee RT, Wagers AJ, and Rubin LL (2014) Vascular and neurogenic rejuvenation of the aging mouse brain by young systemic factors. *Science* **344**:630–634.
- Klein LE, Freeze BS, Smith AB III, and Horwitz SB (2005) The microtubule stabilizing agent discodermolide is a potent inducer of accelerated cell senescence. *Cell Cycle* **4**:501–507.
- Knudsen ES and Witkiewicz AK (2017) The strange case of CDK4/6 inhibitors: mechanisms, resistance, and combination strategies. *Trends Cancer* **3**:39–55.
- Laberge R-M, Awad P, Campisi J, and Desprez P-Y (2012) Epithelial-mesenchymal transition induced by senescent fibroblasts. *Cancer Microenviron* **5**:39–44.
- Le Duff M, Gouju J, Jonchère B, Guillon J, Toutain B, Boissard A, Henry C, Guette C, Lelièvre E, and Coqueret O (2018) Regulation of senescence escape by the cdk4-EZH2-AP2M1 pathway in response to chemotherapy. *Cell Death Dis* **9**:199.
- Lehmann BD, Bauer JA, Chen X, Sanders ME, Chakravarthy AB, Shyr Y, and Pieterpol JA (2011) Identification of human triple-negative breast cancer subtypes and preclinical models for selection of targeted therapies. *J Clin Invest* **121**:2750–2767.
- Milanovic M, Fan DNY, Belenki D, Däbritz JHM, Zhao Z, Yu Y, Dörr JR, Dimitrova L, Lenze D, Monteiro Barbosa IA, et al. (2018) Senescence-associated reprogramming promotes cancer stemness. *Nature* **553**:96–100.
- Mita A, Lockhart AC, Chen TL, Bochinski J, Curtright J, Cooper W, Hammond L, Rothenberg M, Rowinsky E, and Sharma S (2004) A phase I pharmacokinetic (PK) trial of XAA296A (discodermolide) administered every 3 wks to adult patients with advanced solid malignancies (Abstract). *J Clin Oncol* **22**(Suppl 14):2025.
- Morgan WA (1939) Test for the significance of the difference between the two variances IN a sample from a normal bivariate population. *Biometrika* **31**:13–19.
- Nadaradjane C, Yang CH, Rodriguez-Gabin A, Ye K, Sugawara K, Atasoylu O, Smith AB III, Horwitz SB, and McDaid HM (2018) Improved dose-response relationship of (+)-discodermolide-taxol hybrid congeners. *J Nat Prod* **81**:607–615.
- Nieto MA, Sargent MG, Wilkinson DG, and Cooke J (1994) Control of cell behavior during vertebrate development by Slug, a zinc finger gene. *Science* **264**:835–839.
- Ogrunc M, Di Micco R, Liontos M, Bombardelli L, Mione M, Fumagalli M, Gorgoulis VG, and d'Adda di Fagnana F (2014) Oncogene-induced reactive oxygen species fuel hyperproliferation and DNA damage response activation. *Cell Death Differ* **21**:998–1012.
- Olsen LF, Issinger O-G, and Guerra B (2013) The Yin and Yang of redox regulation. *Redox Rep* **18**:245–252.
- Prota AE, Bargsten K, Redondo-Horcajo M, Smith AB III, Yang CH, McDaid HM, Paterson I, Horwitz SB, Fernando Diaz J, and Steinmetz MO (2017) Structural basis of microtubule stabilization by discodermolide. *ChemBioChem* **18**:905–909.
- Samaraweera L, Adomako A, Rodriguez-Gabin A, and McDaid HM (2017) A novel indication for panobinostat as a senolytic drug in NSCLC and HNSCC. *Sci Rep* **7**:1900.
- Samaraweera L, Liu L, Suzuki M, Horwitz SB, and McDaid HM (2012) Senescence reversion contributes to acquired drug resistance (Abstract). *Cancer Res* **72** (Suppl 1):4230.
- Sampah MES, Shen L, Jilek BL, and Siliciano RF (2011) Dose-response curve slope is a missing dimension in the analysis of HIV-1 drug resistance. *Proc Natl Acad Sci USA* **108**:7613–7618.
- Santaguida S, Richardson A, Iyer DR, M'Saad O, Zasadil L, Knouse KA, Wong YL, Rhind N, Desai A, and Amon A (2017) Chromosome mis-segregation generates cell-cycle-arrested cells with complex karyotypes that are eliminated by the immune system. *Dev Cell* **41**:638–651.e5.
- Schafer MJ, White TA, Iijima K, Haak AJ, Ligresti G, Atkinson EJ, Oberg AL, Birch J, Salmonowicz H, Zhu Y, et al. (2017) Cellular senescence mediates fibrotic pulmonary disease. *Nat Commun* **8**:14532.
- Segu VBG, Li G, and Metz SA (1998) Use of a soluble tetrazolium compound to assay metabolic activation of intact beta cells. *Metabolism* **47**:824–830.
- Sharpless NE and Sherr CJ (2015) Forging a signature of in vivo senescence. *Nat Rev Cancer* **15**:397–408.
- Shaw SJ (2008) The structure activity relationship of discodermolide analogues. *Mini Rev Med Chem* **8**:276–284.
- Shaw SJ, Sundermann KF, Burlingame MA, Myles DC, Freeze BS, Xian M, Brouard I, and Smith AB III (2005) Toward understanding how the lactone moiety of discodermolide affects activity. *J Am Chem Soc* **127**:6532–6533.
- Shaw SJ, Sundermann KF, Burlingame MA, Zhang D, Petryka J, and Myles DC (2006) A series of 23,24-dihydrodiscodermolide analogues with simplified lactone regions. *Bioorg Med Chem Lett* **16**:1961–1964.
- Skehan P, Storeng R, Scudiero D, Monks A, McMahon J, Vistica D, Warren JT, Bokesch H, Kenney S, and Boyd MR (1990) New colorimetric cytotoxicity assay for anticancer-drug screening. *J Natl Cancer Inst* **82**:1107–1112.
- Smith AB, Beauchamp TJ, LaMarche MJ, Kaufman MD, Qiu Y, Arimoto H, Jones DR, and Kobayashi K (2000) Evolution of a gram-scale synthesis of (+)-discodermolide. *J Am Chem Soc* **122**:8654–8664.
- Smith AB and Freeze BS (2007) (+)-Discodermolide: total synthesis, construction of novel analogues, and biological evaluation. *Tetrahedron* **64**:261–298.
- Smith AB III, Kaufman MD, Beauchamp TJ, LaMarche MJ, and Arimoto H (1999) Gram-scale synthesis of (+)-discodermolide. *Org Lett* **1**:1823–1826.
- Smith AB III, Rucker PV, Brouard I, Freeze BS, Xia S, and Horwitz SB (2005) Design, synthesis, and biological evaluation of potent discodermolide fluorescent and photoaffinity molecular probes. *Org Lett* **7**:5199–5202.
- Smith AB, Sugawara K, Atasoylu O, Yang CP, and Horwitz SB (2011) Design and synthesis of (+)-discodermolide-paclitaxel hybrids leading to enhanced biological activity. *J Med Chem* **54**:6319–6327.

- Smith AB III and Xian M (2005) Design, synthesis, and biological evaluation of simplified analogues of (+)-discodermolide. Additional insights on the importance of the diene, the C7 hydroxyl, and the lactone. *Org Lett* **7**:5229–5232.
- Storer M, Mas A, Robert-Moreno A, Pecoraro M, Ortells MC, Di Giacomo V, Yosef R, Pilpel N, Krizhanovsky V, Sharpe J, et al. (2013) Senescence is a developmental mechanism that contributes to embryonic growth and patterning. *Cell* **155**: 1119–1130.
- Watson EV and Elledge SJ (2017) Aneuploidy police detect chromosomal imbalance triggering immune crackdown!. *Trends Genet* **33**:662–664.
- Wolff AC (2016) CDK4 and CDK6 inhibition in breast cancer - a new standard. *N Engl J Med* **375**:1993–1994.
- Yang CH, Wang C, Ojima I, and Horwitz SB (2018) Taxol analogues exhibit differential effects on photoaffinity labeling of β -tubulin and the multidrug resistance associated P-glycoprotein. *J Nat Prod* **81**:600–606.
- Ziegler DV, Wiley CD, and Velarde MC (2015) Mitochondrial effectors of cellular senescence: beyond the free radical theory of aging. *Aging Cell* **14**:1–7.
-
- Address correspondence to:** Dr. Hayley M. McDaid, Department of Molecular Pharmacology, Albert Einstein College of Medicine, 1300 Morris Pk Ave, F249b, Bronx, NY 10461. E-mail: hayley.mcdaid@einsteinmed.org
-

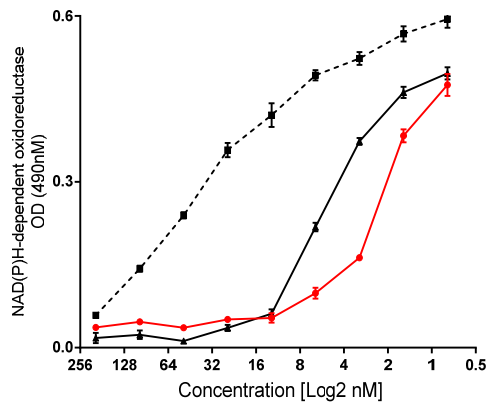
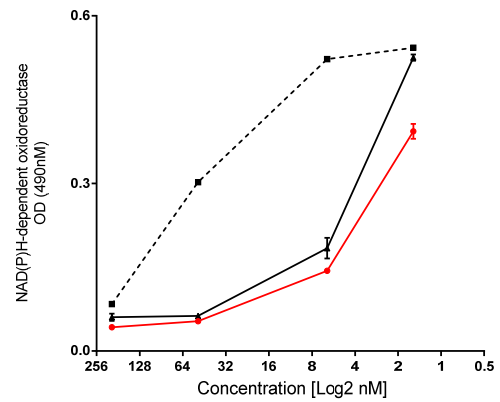
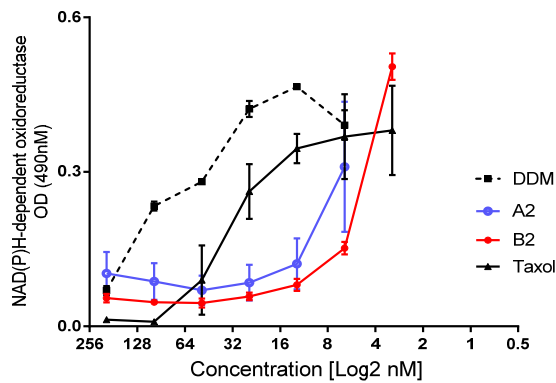
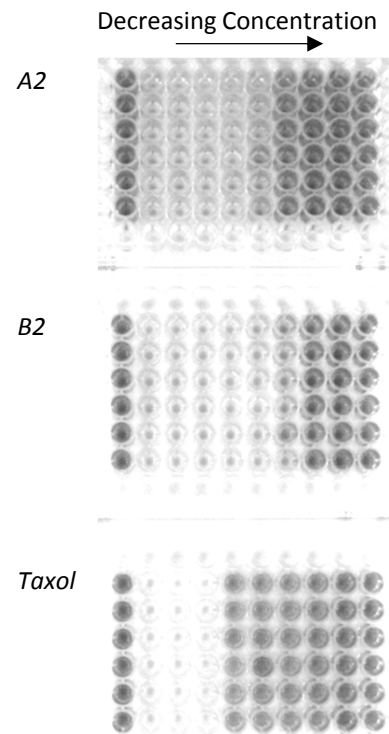
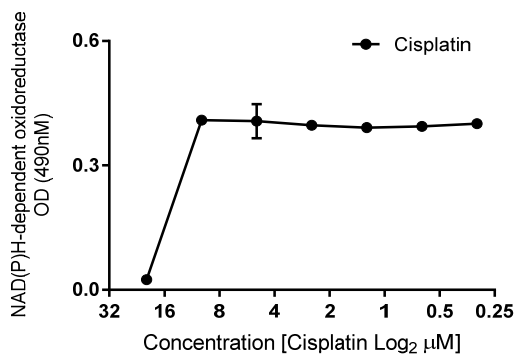
Structural Refinement of the Tubulin Ligand (+)-Discodermolide to Attenuate Chemotherapy-Mediated Senescence

Boying Guo, Alicia Rodriguez-Gabin, Andrea E. Prota, Tobias Mühlethaler, Nan Zhang, Kenny Ye, Michel O. Steinmetz, Susan Band Horwitz, Amos B. Smith III, and Hayley M. McDaid

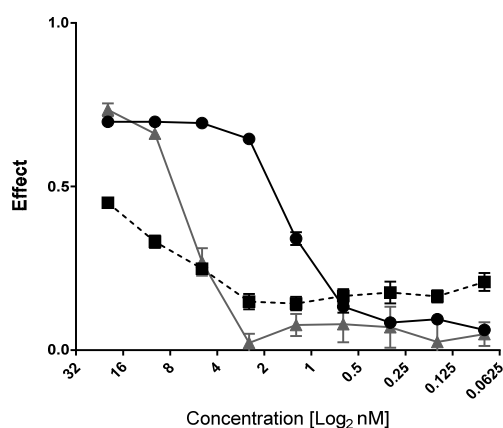
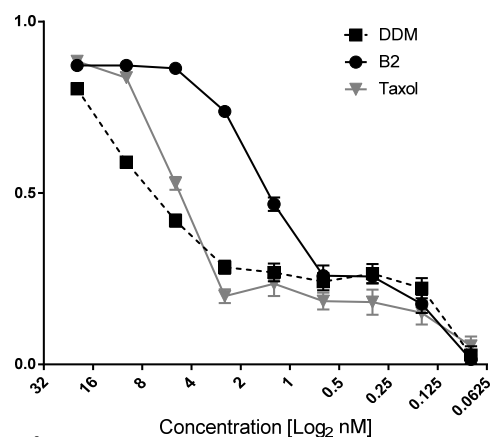
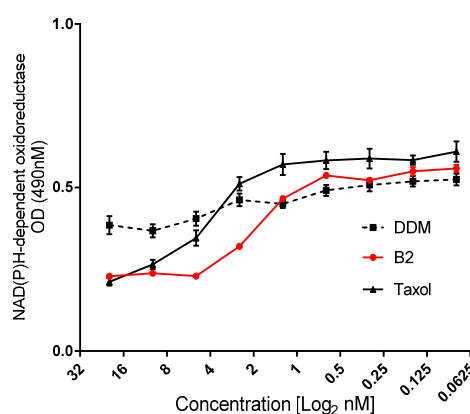
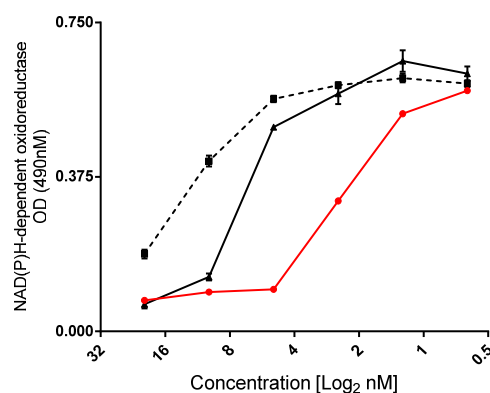
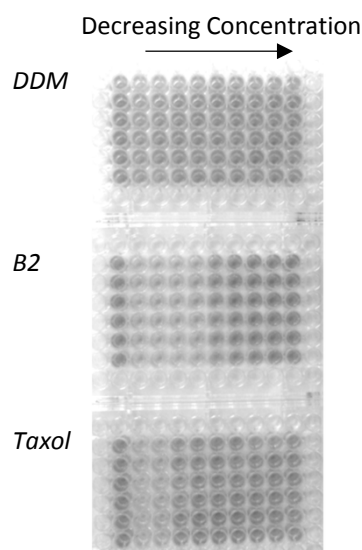
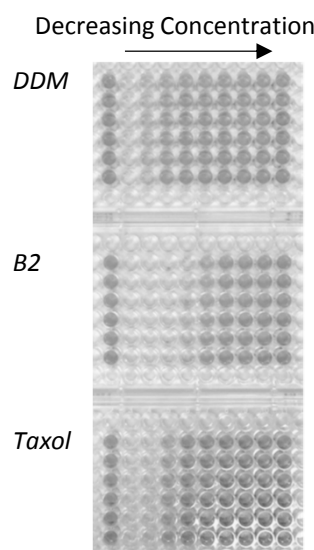


Supplemental Fig. S1 –Distribution of Reactive Oxygen Species in Congener-treated Cancer Cells

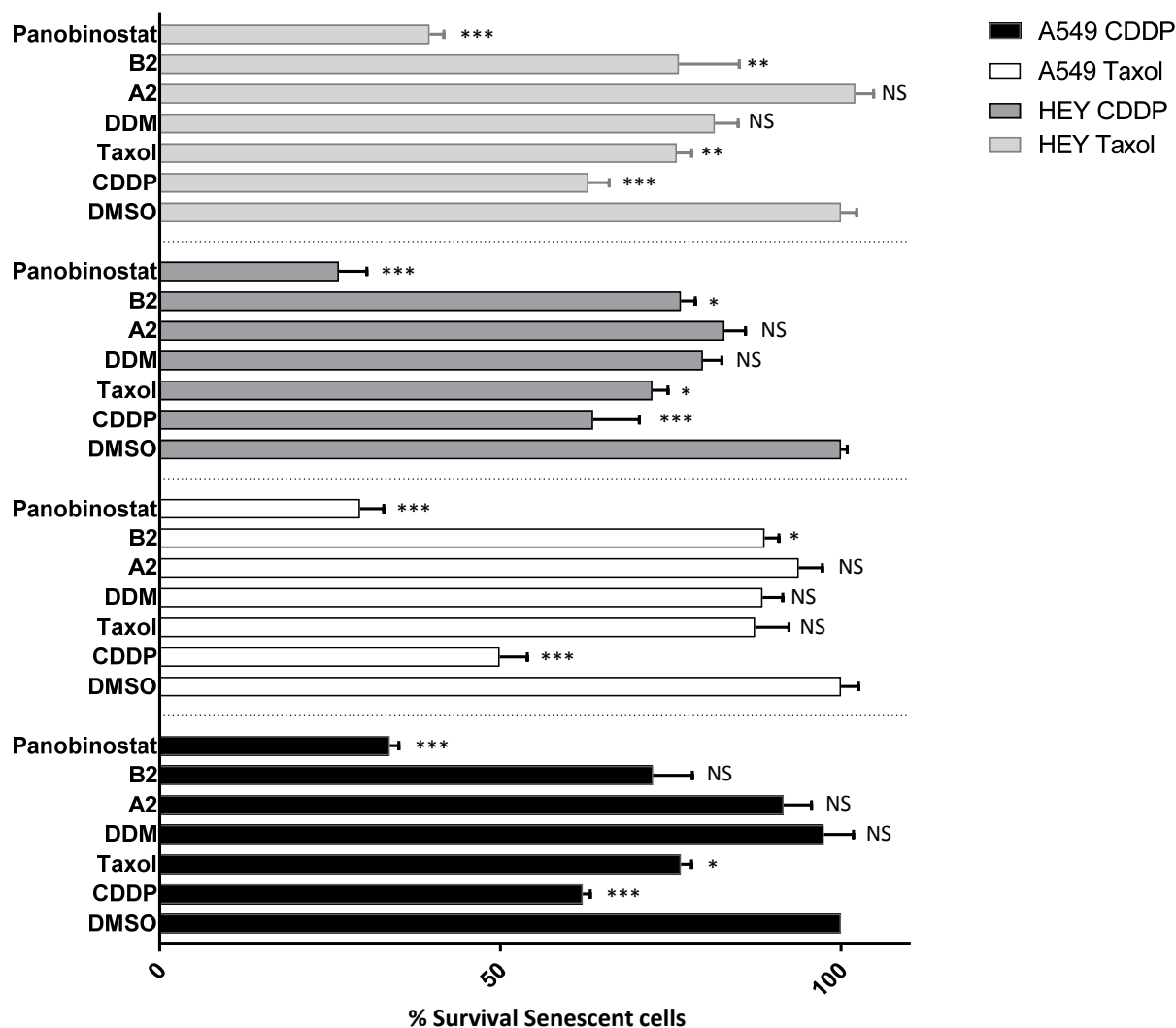
Distribution of log-transformed ROS values among DDM- and congener-treated cells. Line represents median. See Table 1 for experimental and analytical detail.

(A) 3 days**(B) 6 days****(C) 21 days****(D) 21 days****(E) 21 days – CDDP****Supplemental Fig. S2 - Superior Long-Term Efficacy of Congener B2 in HEY Cells**

Dose-response curves for DDM, B2 or Tx (administered once) in the Ovarian cancer cell line HEY after (A) 3 cell doublings (3 days), (B) 6 days (when SA-βGal assessments for senescence were performed), and (C) 21 days. Note that 21 day include data for congener A2, found to have weaker long-term efficacy relative to B2. MTS assays (NAD(P)H-dependent oxidoreductase activity) were used to determine viability and data expressed as OD @490nm ± SEM for the dose range indicated. Low OD correlates with low cell viability, and thus potent congener activity. (D) Representative images of SRB-stained plates showing superior sustained anti-tumor efficacy of B2 versus A2 at 21 days post-dosing. (E) Anti-tumor efficacy of cisplatin-treated HEY cells (starting dose 20μM) for 21 days, indicating weak long-term anti-cancer effect.

(A) 4 days**(B) 24 days****(C) 4 days****(D) 24 days****(E)****(F)****Supplemental Fig. S3 - Superior Long-Term Efficacy of Congener B2 in SKOV3 cells**

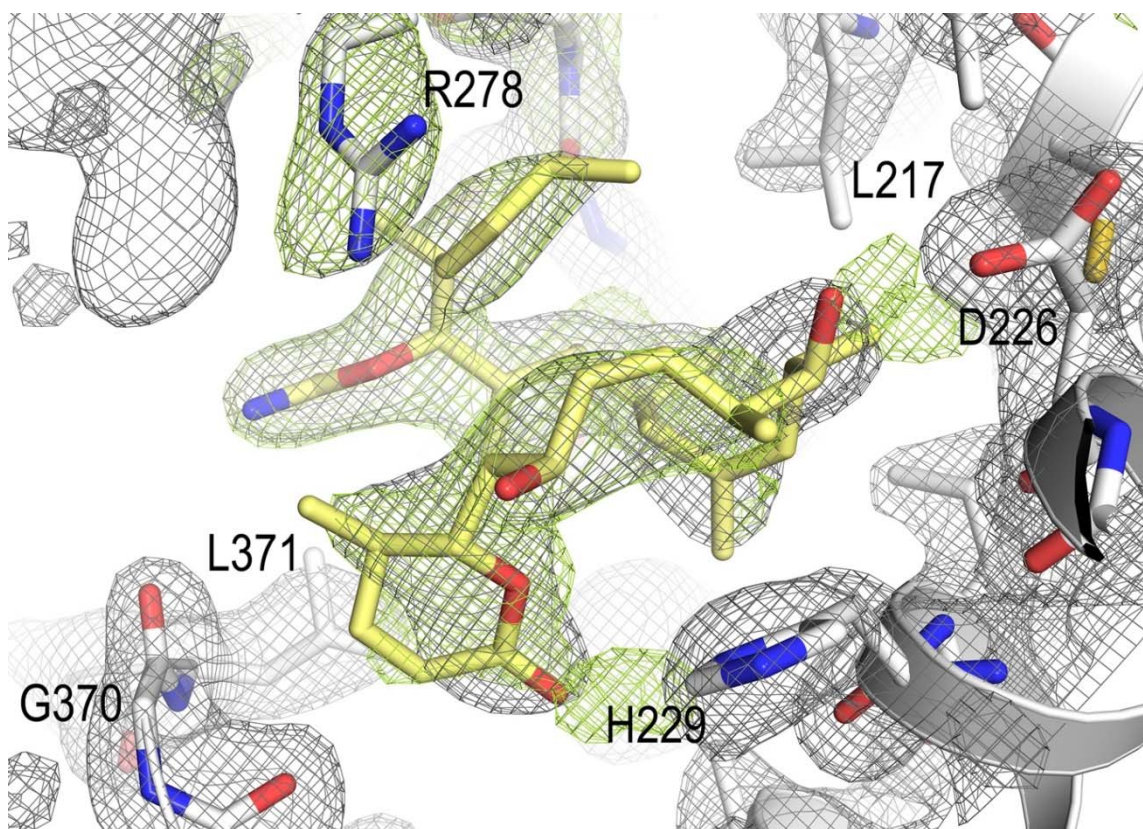
Dose-response curves for DDM, B2 and Taxol in SKOV3 cells after (A) 3 cell doublings (4 days) and (B) 24 days using the SRB assay, and after (C) 3 cell doublings (4 days) and (D) 24 days using the MTS. Representative images of SRB-stained plates corresponding to (E) 4 days and (F) 24 days are shown. Congener B2 had superior anti-tumor efficacy compared to Taxol or DDM.



Supplemental Fig. S4 – Lead Congeners A2 and B2 Do Not Possess Significant Senolytic Activity

A549 (NSCLC) and HEY (ovarian) cancer cells were treated with either Taxol (25nM – A549: 100nM – HEY) or CDDP (12μM both cell lines) for 14 days weeks to induce senescence. Doses were previously established for induction of stable CIS. Surviving senescent cells were subsequently washed and treated with (i) Taxol or CDDP (at the same dose), (ii) DDM or congeners (20nM), or (iii) the HDAC inhibitor panobinostat (100nM), previously demonstrated to have senolytic activity. Cell survival was determined after 3 days of treatment by MTS and data expressed as % survival of senescent cells relative to DMSO-treated control. Statistical significance relative to DMSO-treated cells is indicated (2-way ANOVA with Dunnett's multiple comparisons test, 95% confidence).

As demonstrated previously, panobinostat and CDDP had statistically significant senolytic activity. DDM and congeners, like Taxol, had little to no senolytic activity. No statistical difference was observed for senolytic effect in DDM versus congeners A2 or B2 (2-way ANOVA with Dunnett's multiple comparisons test, 95% confidence).



Supplemental Fig. S5 – Simulated annealing electron density omit map highlighting the validity of the model. The 2mFo-DFc direct electron density map is contoured at 1.0 σ (dark grey), the mFo-DFc difference electron density map is contoured at 3.0 σ (green). Both the interacting residues and the superimposed MX-3-247 molecule (yellow) are in stick representation. The maps were calculated excluding the atoms corresponding to MX-3-247 only.

Cancer Histology / Subtype	Cell Line	E _{Max}											AUC											EC ₅₀ (Log ₂)										
		Disco	Taxol	A1	A2	A3	B1	B2	B3	C1	C2	C3	Disco	Taxol	A1	A2	A3	B1	B2	B3	C1	C2	C3	Disco	Taxol	A1	A2	A3	B1	B2	B3	C1	C3	C3
BREAST CANCER																																		
TNBC																																		
BL1	HCC1143	0.8050	0.8033	0.8362	0.8372	0.7474	0.8629	0.8163	0.6829	0.8468	0.8315	0.6575	3.4797	5.4852	5.3849	5.9579	2.5234	5.6832	5.7053	1.2326	5.4030	3.1522	1.3282	3.7701	1.0519	1.5063	0.7248	4.5905	1.3435	0.9376	6.2485	1.5816	4.1962	5.9699
	HCC38	0.8701	0.8385	0.8952	0.8847	0.8733	0.8861	0.8752	0.8682	0.8811	0.8965	0.8580	3.9687	7.0270	5.8863	6.0467	3.0025	6.0012	6.1506	1.5459	5.1699	3.7787	1.5408	3.4797	-0.4296	1.2047	1.0064	4.5302	0.7664	0.7270	6.2475	2.0952	3.7552	6.3712
	HCC1937	0.6270	0.6140	0.5643	0.5378	0.6200	0.6101	0.5806	0.5924	0.5231	0.5649	0.5611	3.5342	3.9447	3.5651	3.6597	2.5663	4.0929	4.0344	1.6292	3.2862	2.9142	1.5223	3.1881	2.4345	2.3916	1.6594	4.8537	1.8318	1.5236	6.2235	2.6542	3.7999	6.2924
BL2	SUM149PT	0.8879	0.8760	0.8751	0.8894	0.7910	0.8721	0.8809	0.8147	0.8926	0.8926	0.8211	3.9507	6.1278	5.7585	5.9274	3.2228	5.6256	6.2245	1.9473	5.3538	4.0840	1.8247	4.0288	0.6712	1.1511	1.1791	4.7547	1.4320	0.6689	5.8970	1.8927	3.3998	5.9679
M	HS578T	0.8573	0.9028	0.9532	0.9534	0.9267	0.9458	0.9581	0.5950	0.9624	0.9498	0.7078	3.6836	4.2257	4.9315	6.2574	2.6180	5.7237	6.3708	1.1805	5.0782	3.0813	1.1551	4.3818	2.9522	2.8231	1.2359	5.4198	1.8616	1.1544	7.4617	2.6781	4.8176	7.1348
	MDA-MB-436	0.9159	0.9159	0.9398	0.9316	0.9513	0.9079	0.9137	0.9159	0.9345	0.9262	0.9471	3.8985	6.4343	5.8235	6.7278	3.7432	5.9370	6.7277	2.9867	6.4115	5.4797	3.1964	2.8618	0.7153	1.7033	0.5052	4.0389	1.4047	0.1616	4.7097	0.9532	2.0224	4.6608
	BT549	0.9233	0.9514	0.9378	0.9302	0.9134	0.9378	0.9286	0.8896	0.9166	0.9151	0.9163	3.3247	5.8956	5.6491	6.3699	3.6550	5.5435	6.4266	2.4385	5.5527	5.0716	2.9415	4.5347	1.7108	1.8797	0.9884	3.9740	1.9811	0.7913	5.2344	1.9062	2.4209	4.7666
OVARIAN CANCER	HEY	0.5477	0.8847	0.9091	0.8931	0.9279	0.8922	0.9022	0.3990	0.8783	0.9182	0.8871	1.2638	6.7751	5.3381	6.3969	4.3811	3.5552	6.1725	0.5308	5.4767	5.4724	3.1664	4.3387	-0.6259	2.0074	0.4731	3.2809	1.6003	0.4812	5.0710	1.5842	1.9078	4.5965
	HEYTx100	0.9318	0.8190	0.9274	0.9481	0.9496	0.8957	0.9324	0.3224	0.9440	0.9485	0.4472	3.3403	1.8476	3.6322	4.8346	2.2614	3.6489	4.8639	0.1673	4.0891	2.0920	0.7066	5.1476	6.9853	4.0526	2.8472	5.7431	3.8921	3.2356	8.2851	3.6665	5.8817	8.2189
	IGROV	0.7721	0.7974	0.7957	0.8036	0.6786	0.8237	0.8642	0.7766	0.8330	0.8010	0.8048	3.8286	5.9548	5.1993	5.6258	3.4370	5.5477	6.2174	2.9156	5.5839	4.8479	3.1545	3.7868	0.3703	0.4286	-1.1475	2.9541	0.3434	-1.3781	4.2402	0.8923	1.7638	4.2194
	SKOV3	0.7099	0.8424	0.8619	0.8306	0.8225	0.8418	0.8183	0.8563	0.8630	0.8568	0.8230	1.9132	5.4413	5.2976	5.5561	2.7955	4.4344	6.0526	2.2836	4.9632	4.4309	1.9337	6.5657	1.1201	2.2053	1.1830	4.5624	3.6876	0.2852	5.2844	2.1737	2.7915	5.6091
	SKVLB	0.4607	0.1966	0.5488	0.5528	0.3085	0.6382	0.6604	0.1979	0.5888	0.4353	0.2172	1.5771	0.9624	1.8509	2.2224	1.1844	2.2535	2.6048	0.4353	1.9626	1.1919	0.5356	5.6492	5.4340	7.0358	7.3182	8.1731	6.2336	7.0242	6.7933	7.1308	8.5273	8.5038

Supplemental Table S1: Median dose-response parameters for Taxol, DDM and Congeners in individual cancer cell lines

TNBC – Triple negative breast cancer

BL1: Basal-like 1

BL2: Basal-like 2

M: Mesenchymal

Values for Taxol are shaded in blue

AUC

Analysis	Significant?	Summary	Adjusted P Value
Disco vs. Taxol	Yes	**	0.0061
Disco vs. A2	Yes	****	<0.0001
Disco vs. B1	Yes	****	<0.0001
Disco vs. B2	Yes	****	<0.0001
Taxol vs. A2	No	ns	0.1903
Taxol vs. B1	No	ns	0.6662
Taxol vs. B2	No	ns	0.0819

EC50

Analysis	Significant?	Summary	Adjusted P Value
Disco vs. Taxol	Yes	**	0.0017
Disco vs. A2	Yes	***	0.0002
Disco vs. B1	Yes	****	<0.0001
Disco vs. B2	Yes	***	0.0002
Taxol vs. A2	No	ns	0.4497
Taxol vs. B1	No	ns	0.4578
Taxol vs. B2	No	ns	0.2149

EMAX

Analysis	Significant?	Summary	Adjusted P Value
Disco vs. Taxol	No	ns	0.7891
Disco vs. A2	No	ns	0.0892
Disco vs. B1	No	ns	0.0555
Disco vs. B2	No	ns	0.0607
Taxol vs. A2	No	ns	0.1734
Taxol vs. B1	No	ns	0.1488
Taxol vs. B2	No	ns	0.1683

SUPPLEMENTAL TABLE S2 - Pairwise t-test for Dose-Response Parameters

DRUG	Parameter			Parameter		
	Median AUC	SD (AUC)	P Var (AUC) vs. Taxol	Median E _{Max}	SD (E _{max})	P Var (E _{max}) vs. Taxol
Disco	3.50695	0.97706615	0.016956002	0.83115	0.157390523	0.199148188
Taxol	5.6904	1.92317383	NA	0.84045	0.204525746	NA
A1	5.31785	1.223496332	0.074511944	0.88515	0.138888834	0.107488209
A2	5.94265	1.311144697	0.10978931	0.88705	0.142357313	0.122490065
A3	2.899	0.828108304	0.004728127	0.8479	0.18764275	0.390061093
B1	5.5456	1.211258387	0.070235719	0.8791	0.10813476	0.022555494
B2	6.16155	1.210598611	0.070009702	0.87805	0.114214531	0.032853267
B3	1.58755	0.944414673	0.013198467	0.72975	0.241689694	0.705435886
C1	5.26185	1.204173532	0.067832837	0.8797	0.138383169	0.105392502
C2	3.93135	1.356894323	0.131375618	0.89455	0.161974231	0.225738015
C3	1.68275	0.971666555	0.01628463	0.81295	0.217761783	0.580528738

Supplemental Table 3 - F Statistic Probability for AUC and E_{max} (relative to Taxol)

NA - Not applicable

Taxol Resistant Cell Lines (Highlighted)

Cell Line	Hill Slope	AUC
HCC1143	1.7056	5.4852
HCC38	1.2311	7.027
HCC1937	0.71	3.9447
SUM149PT	1.1958	6.1278
HS578T	0.5129	4.2257
MDA-MB-436	1.418	6.4343
BT549	1.403	5.8956
HEY	1.0638	6.7751
HEYTx100	0.9843	1.8476
IGROV	1.4903	5.9548
SKOV3	0.4823	5.4413
SKVLB	0.2902	0.9624

Paired t-test - Resistant Cancer Cells

AUC

Analysis	Significant?	Summary	Adjusted P Value
Disco vs. Taxol	No	ns	0.0546
Disco vs. A2	No	ns	0.4808
Disco vs. B1	No	ns	0.9996
Disco vs. B2	No	ns	0.133
Taxol vs. A2	Yes	**	0.017
Taxol vs. B1	No	ns	0.1868
Taxol vs. B2	Yes	**	0.0072

EC50

Analysis	Significant?	Summary	Adjusted P Value
Disco vs. Taxol	No	ns	0.0811
Disco vs. A2	No	ns	0.4796
Disco vs. B1	No	ns	0.3978
Disco vs. B2	No	ns	0.2588
Taxol vs. A2	No	**	0.0075
Taxol vs. B1	No	ns	0.4847
Taxol vs. B2	No	*	0.0287

EMAX

Analysis	Significant?	Summary	Adjusted P Value
Disco vs. Taxol	No	ns	0.2341
Disco vs. A2	No	ns	0.3352
Disco vs. B1	No	ns	0.7181
Disco vs. B2	No	ns	0.674
Taxol vs. A2	No	ns	0.3383
Taxol vs. B1	No	ns	0.0528
Taxol vs. B2	No	ns	0.2503

Supplemental Table 4 - Annotation of Taxol Resistant Cell Lines and paired t-test of Dose-Response Parameters in Resistant Versus Sensitive Cell Lines.

DRUG	DRUG DOSE (nM)								
(A) % Senescent cells at 6 days: SA-βGal+ and morphologically enlarged with dense, granular cytoplasm									
	200nM		50nM		6.25nM		1.25nM		Concentration
	χ	SD	χ	SD	χ	SD	χ	SD	
DDM	34.944	5.821	36.333	2.603	0.680	0.020	0.150	0.076	
B2	23.343	3.138	36.443	9.163	24.888	4.743	2.344	0.580	
Taxol	9.748	0.641	10.225	6.532	2.023	0.526	1.325	0.686	

(B) Drug effect (%) : 6 day SRB assay

	200nM		50nM		6.25nM		1.25nM		Concentration
	χ	SD	χ	SD	χ	SD	χ	SD	
DDM	86.100	0.312	50.100	3.500	13.800	4.300	10.400	5.120	
B2	92.900	0.700	91.200	0.760	76.300	2.340	35.100	3.230	
Taxol	90.010	1.400	89.600	2.580	69.600	4.540	13.330	6.230	

(C) % Adherent cells (100 - Drug effect [from B])

	200nM		50nM		6.25nM		1.25nM		Concentration
DDM	13.900		49.900		86.200		89.600		
B2	7.100		8.800		23.700		64.900		
Taxol	9.990		10.400		30.400		86.670		

(D) Proportion of adherent cells that are senescent (% of adherent cells [C] that are SA-βGal+ [A])

	200nM	<i>P</i> value #	50nM	<i>P</i> value #	6.25nM	<i>P</i> value #	1.25nM	<i>P</i> value #	Concentration
DDM	4.857		18.130		0.586		0.134		
B2	1.657	NS	3.207	*	5.898	*	1.521	NS	
Taxol	0.974	**	1.063	*	0.615	NS	1.148	NS	

Statistical test: 2 way ANOVA (relative to DDM) with Turkey's test

(E) Proportion of adherent cells that are NOT senescent (% of adherent cells [C] that are SA+βGal- [D])

	200nM		50nM		6.25nM		1.25nM		Concentration
DDM	9.043		31.770		85.614		89.466		
B2	5.443		5.593		17.802		63.379		
Taxol	9.016		9.337		29.785		85.522		

Senescent data were derived from day 6 post-treatment HEY cells
 A series of calculations (A to E) was used to compute the proportion of adherent senescent and non-senescent cells at 6 days post-treatment.

Supplemental Table S5 - Computation of % Senescent (% SA-βGal+) in HEY Cells as a Proportion of Drug effect

T ₂ R-TTL-B2	
Data collection*	
Space group	P2 ₁ 2 ₁ 2 ₁
Cell dimensions	
<i>a</i> , <i>b</i> , <i>c</i> (Å)	104.1, 157.2, 178.4
Resolution (Å)	49.4-2.0 (2.05-2.00)
<i>R</i> _{merge} (%)	19.5 (532.1)
<i>R</i> _{meas} (%)	20.3 (553.7)
<i>R</i> _{pim} (%)	6.2 (153.7)
<i>I</i> / σ <i>I</i>	10.8 (0.6)
CChalf	99.9 (18.9)
Completeness (%)	99.9 (99.3)
Redundancy	13.5 (12.9)
Refinement	
Resolution (Å)	49.4-2.0
No. unique reflections	196846
<i>R</i> _{work} / <i>R</i> _{free}	19.9 / 24.3
No. atoms	
Protein	17176
Ligands	360
Water	1260
Average <i>B</i> -factors (Å ²)	
Protein	61.0
Ligand (chain B / D)	96.4 / 71.6
Water	64.5
Wilson <i>B</i> -factor	42.1
R.m.s. deviations	
Bond lengths (Å)	0.003
Bond angles (°)	0.562
Ramachandran statistics ^c	
Favored regions (%)	97.7
Allowed regions (%)	2.3
Outliers (%)	0

Supplemental Table S6

X-ray data collection and refinement statistics for B2

*The structure data were collected from a single crystal. Values in parentheses are for highest-resolution shell.

SUPPLEMENTAL METHODS

Part 1 – Chemical Synthesis of DDM Congeners.

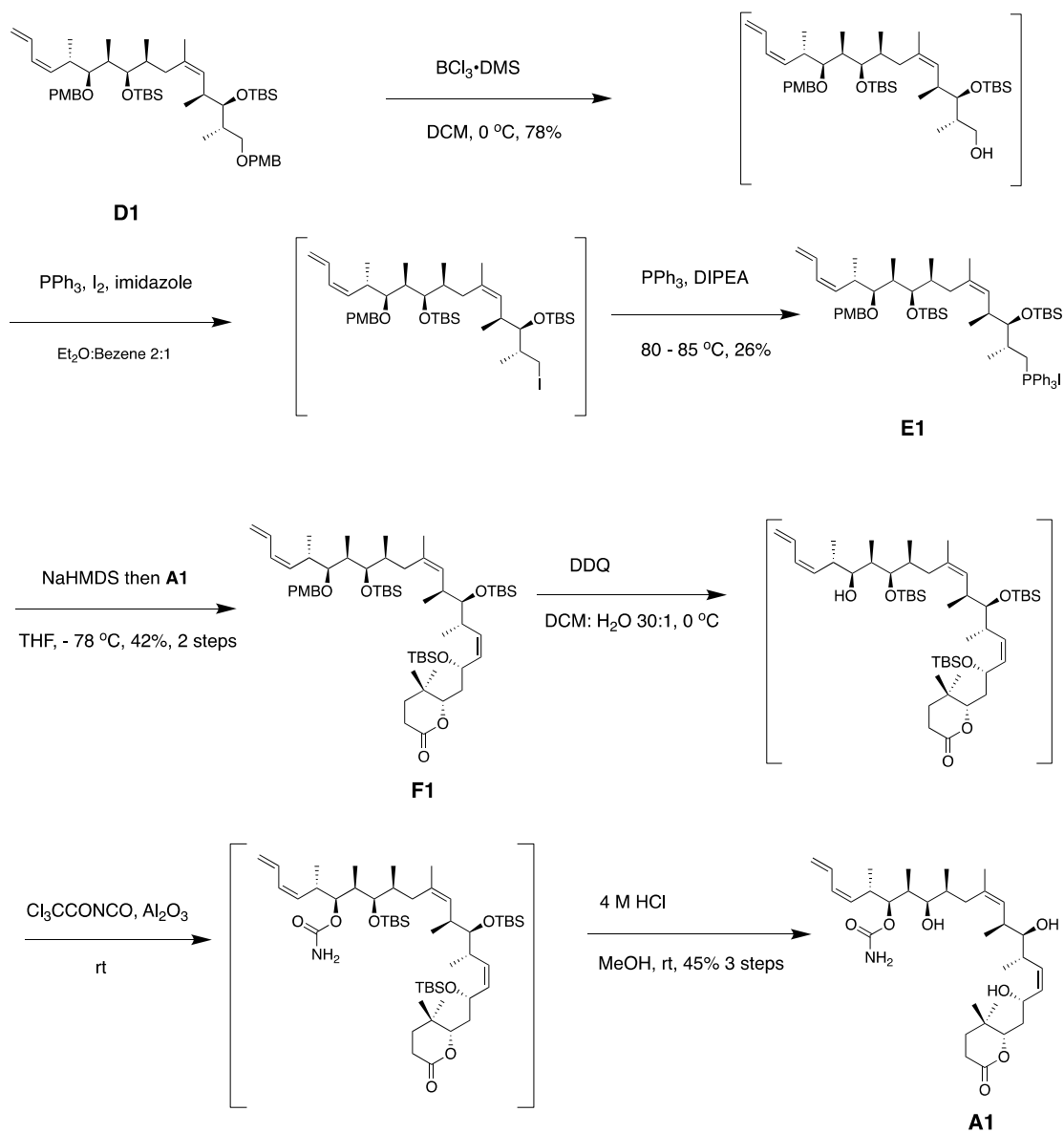
General Information

All chemicals were purchased from Sigma Aldrich, Acros Organics, or TCI America, unless otherwise noted. Anhydrous diethyl ether (Et_2O), dichloromethane (CH_2Cl_2) and toluene were acquired from a Pure Solve PS-400 system. Tetrahydrofuran (THF) was distilled from Sodium/benzophenone. Diisopropylethylamine (DIPEA) was distilled over calcium hydride under a nitrogen atmosphere.

Reactions

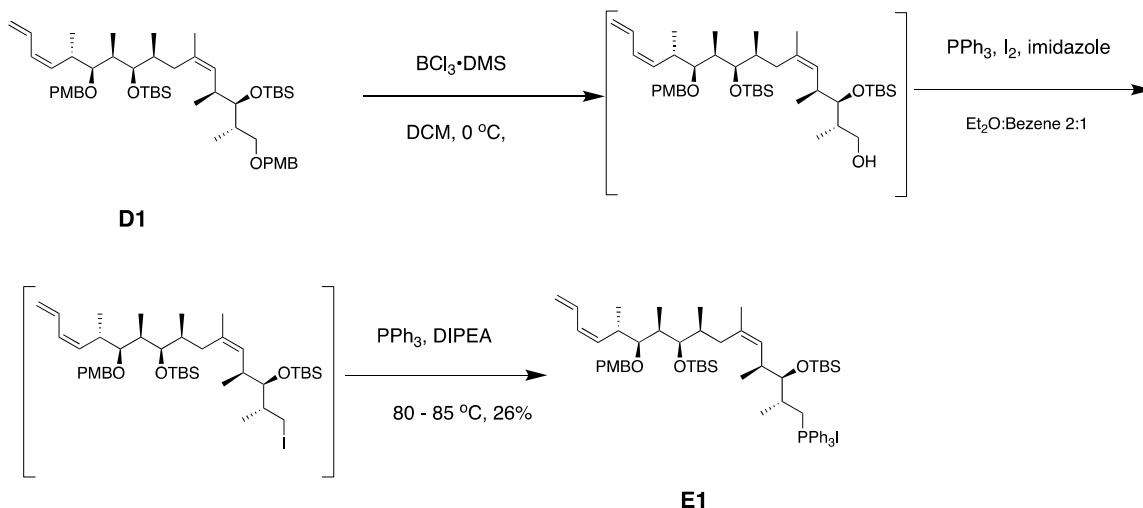
These were performed under the protection of argon otherwise noted and were monitored using thin layer chromatography (TLC) with 250 mm pre-coated silica gel plates purchased from Silicycle Technology. Silica gel flash chromatography was conducted using ACS grade solvents and silica gel that was purchased from Silicycle Technology. Medium pressure liquid chromatography was conducted by using a Varian ProStar 210 Pump equipped with a high-pressure glass column (350 mm \times 35 mm or 350 mm \times 10 mm) packed with silica gel (Sorbent Technologies, Standard Grade, porosity 60 Å, particle size 32-63 μm). All Infrared spectra were recorded on a Jasco Model FT/IR-480 Plus spectrometer. All optical rotations were measured on a Jasco P-2000 polarimeter. ^1H NMR and ^{13}C NMR spectra were recorded on Bruker Avance III 500 MHz spectrometer equipped with either an Oxford cryomagnet or a Spectrospin/Bruker cryomagnet (500MHz/52mm) with a 5-mm dual cryo probe using either 5 mm or 3 mm NMR tubes. High-resolution mass spectra (HRMS) were acquired either on a Waters LC-TOF mass spectrometer (model LCT-XE Premier) or on a waters GCT Premier spectrometer at the University of Pennsylvania.

Representative Synthesis of Disco-analog A1:*



* intermediates in bracket were not fully characterized either due to the instability or inseparable impurities.

General Procedure for the Preparation of Wittig Phosphonium Salt.

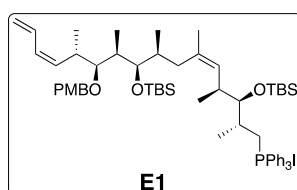


To a 50 ML round-bottomed flask containing **D1**¹ (230 mg, 0.276 mmol, 1 equiv.), 30 ML of DCM and a magnetic stirring bar were introduced sequentially. The resultant clear solution was cooled with stirring to 0 °C by standing in an ice-bath for 5 minutes. At this stage, BCl₃-DMS complex (1.0 M in DCM, 0.145 ML, 0.290 mmol, 1.05 equiv.) was introduced slowly via syringe. After the addition, the reaction was stirred for another 15 minutes at 0 °C and quenched with the addition of 10 ML of sat. NaHCO₃. The organic layer was separated. The aqueous layer was extracted with DCM 2 X 20 ML. The combined organic layers were washed sequentially with DI water 20 ML and sat. NaCl 20 ML, and dried over MgSO₄. After removal of MgSO₄ by filtration, the filtrate was concentrated under vacuum on a rotavapor with the temperature of the water bath below 30 °C. The alcohol product was used as crude in the next step without further purification.²

The prepared alcohol product was re-dissolved in 45 ML of premixed solvent of diethyl ether and benzene (v:v=2:1). PPh₃ (86 mg, 0.331 mmol, 1.2 equiv.) and imidazole (26.3 mg, 0.386 mmol, 1.4 equiv.) and a magnetic stirring bar were added sequentially. The resultant suspension was vigorously stirred at room temperature for 5 minutes. At the stage, a solution of iodine (84 mg, 0.331 mmol, 1.2 equiv.) in 5 ML of the premixed solvent of diethyl ether and benzene (v:v=2:1) was introduced dropwise. Reaction solution became cloudy rapidly following the addition of iodine. In some cases, a white precipitate could be formed at the bottom of the reaction flask. After the addition of iodine, the reaction was stirred at room temperature for another 2 hours or till no starting material was observed using TLC. Then the reaction was quenched by the addition of 20 ML of sat. NaHCO₃. After separation, the aqueous layer was extracted by diethyl ether 40 ML. The combined organic layers were washed sequentially with sat. NaHSO₃ 20 ML, DI water 20 ML and sat. NaCl 20 ML and dried over Na₂SO₄. After the removal of Na₂SO₄ by filtration, the filtrate was concentrated on rotavapor with the

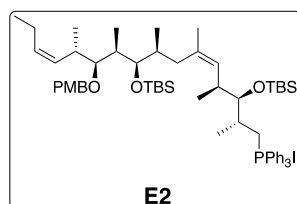
temperature of water bath at 0 °C. The iodide product was used without purification in the next step due to its instability at room temperature.

To the round bottom flask containing the crude iodide, Ph_3P (1085.9 mg, 4.14 mmol, > 15 equiv.) and freshly distilled DIPEA (345 mg, 0.441 ML, 2.67 mmol, > 10 equiv.) and a magnetic stirring bar were introduced sequentially. The flask was purged with argon for 10 minutes, sealed with rubber septa and immersed in a preheated oil bath at 80 °C. The temperature of the oil bath was controlled at 80 to 85 °C at which temperature the triphenylphosphine was melted. The reaction mixture was heated for 20 h and cooled to room temperature. The wax-like solid material was dissolved in minimal amount of DCM and loaded directly to chromatography column for purification.



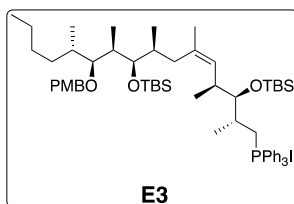
Wittig phosphonium salt **E1** (**Figure 1, E1**): The entitled compound was prepared from **D1** using the general procedure and was purified by column chromatography column on silica gel (Acetonitrile: DCM = 0:100 -> 20:80) as a slightly yellow solid when azeotroped with benzene and dried under high vacuum (24% over 3 steps).

Compound **E1** is known.³



Wittig phosphonium salt **E2** (**Figure 1, E2**): The entitled compound was prepared from **D2** using the general procedure and was purified by column chromatography on silica gel (Acetonitrile: DCM = 0:100 -> 20:80) as a slightly yellow solid when azeotroped with benzene and dried under high vacuum (26% over 3 steps).

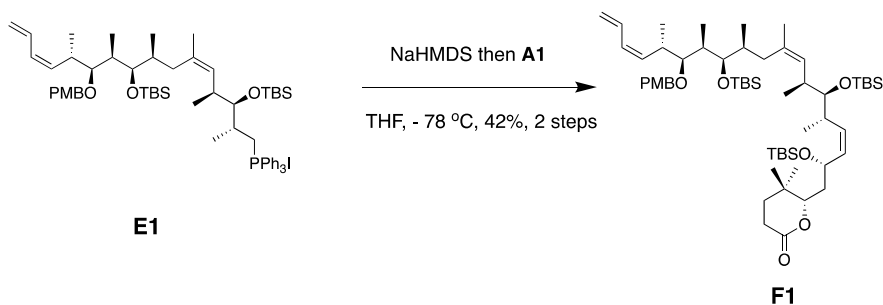
Compound **E2** is known.³



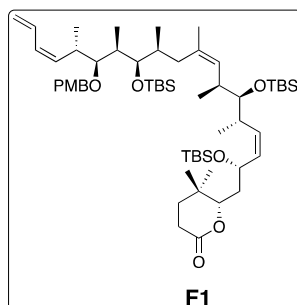
Wittig phosphonium salt **E3** (**Figure 1, E3**): The entitled compound was prepared from **D2** using the general procedure and was purified by column chromatography (Acetonitrile: DCM = 0:100 -> 20:80) as a slightly yellow solid when dried under high vacuum (30% over 3 steps).

Compound **E3** is known.³

General Procedure for the Wittig Olefination.



To a 25 ML of three-necked round-bottomed flask that containing the Wittig phosphonium salt **E1** (180 mg, 0.165 mmol, 1 equiv.) and a magnetic stirring bar, freshly distilled THF 10 ML was introduced. The mixture was simply stirred at room temperature for 5 minutes before it was cooled to - 78 °C by standing in an acetone-dry ice bath for 10 minutes. At this stage, NaHMDS (0.5 M in MTBE, 0.33 ML, 0.165 mmol, 1 equiv.) was introduced slowly resulting a clear orange colored solution. The solution was continued to stir at - 78 °C for 45 minutes. A solution of aldehyde **A1** (51.8 mg, 0.165 mmol, 1 equiv.) in THF 2 ML was added dropwise via syringe at the same temperature. During the addition, the orange color would decay into yellow. The reaction was stirred at - 78 °C for 1 hour then immersed in an acetonitrile-dry ice bath at - 40 °C and stirred at that temperature for another 2 hours before it was quenched by the addition of sat. NH_4Cl 4 ML. After separation, the aqueous layer was extracted with EtOAc 3 X 10 ML. The combined organic layer was washed sequentially with DI water 10 ML, sat. NaCl 10 ML and dried over MgSO_4 . The entitled compound was purified by column chromatography.



Olefin **F1** (**Figure 1, F1**): The entitled compound was prepared from **F1** using the general procedure and was purified by column chromatography (EtOAc:Hexanes = 0:100 → 5:95) as a clear oil (42%).

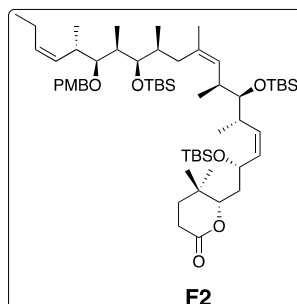
¹H NMR: (500 MHz, Chloroform-*d*) δ 7.26 (q, *J* = 5.7, 5.3 Hz, 2H), 6.89 – 6.79 (m, 2H), 6.59 (dt, *J* = 17.1, 10.6 Hz, 1H), 6.01 (t, *J* = 11.1 Hz, 1H), 5.57 (t, *J* = 10.5 Hz, 1H), 5.30 – 5.15 (m, 3H), 5.12 (d, *J* = 10.3 Hz, 1H), 5.03 (d, *J* = 9.8 Hz, 1H), 4.75 – 4.62 (m, 1H), 4.55 (d, *J* = 10.5 Hz, 1H), 4.47 (d, *J* = 10.6 Hz, 1H), 4.23 (dd, *J* = 10.6, 2.0 Hz, 1H), 3.78 (d, *J* = 3.4 Hz, 3H), 3.44 (dd, *J* = 5.6, 3.5 Hz, 1H), 3.24 (dq, *J* = 7.5, 4.8, 4.0 Hz, 2H), 2.99 (ddt, *J* = 10.9, 7.5, 3.8 Hz, 1H), 2.68 – 2.55 (m, 1H), 2.55 – 2.37 (m, 3H), 2.01 (t, *J* = 12.2 Hz, 1H), 1.89 – 1.44 (m, 13H), 1.10 (t, *J* = 6.1 Hz, 4H), 1.00 (d, *J* = 6.9 Hz, 3H), 0.94 (d, *J* = 4.1 Hz, 17H), 0.88 (dd, *J* = 18.8, 4.4 Hz, 30H), 0.71 (d, *J* = 6.7 Hz, 3H), 0.13 – 0.06 (m, 9H).

¹³C NMR: (126 MHz, CDCl₃) δ 170.35, 158.00, 133.30, 131.87, 131.14, 130.83, 130.19, 130.15, 128.12, 128.05, 116.65, 112.64, 83.57, 81.86, 79.35, 76.25, 76.03, 76.00, 75.75, 74.03, 63.74, 54.24, 39.03, 37.34, 36.62, 34.80, 34.41, 34.29, 34.11, 33.88, 30.57, 30.55, 26.60, 25.51, 25.28, 25.18, 24.83, 24.26, 21.94, 21.64, 18.91, 17.68, 17.59, 17.36, 17.09, 15.88, 15.48, 13.87, 13.11, 9.51, -4.21, -4.29, -4.33, -5.22, -5.36, -5.91;

IR (*V*_{max}, *CM*⁻¹): 2960, 2920, 1752, 1461, 1250, 1096, 830, 774;

[α]_D²³ + 29.94 (*c* 1.25 in CH₂Cl₂);

HRMS (ESI) calcd. For C₅₈H₁₀₄O₇Si₃ *m/z* 996.7090, found 996.7082.



Olefin **F2** (**Figure 1, F2**): The entitled compound was prepared from **F2** using the general procedure and was purified by column chromatography (EtOAc:Hexanes = 0:100 -> 5:95) as a clear oil (35%).

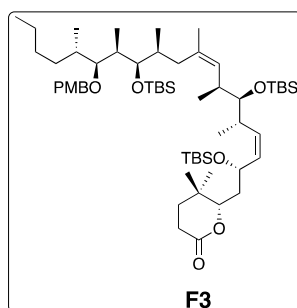
¹H NMR: (500 MHz, Chloroform-d) δ 7.30 – 7.22 (m, 2H), 6.89 – 6.81 (m, 2H), 5.45 (ddt, J = 11.1, 7.8, 1.5 Hz, 1H), 5.36 (dt, J = 10.9, 7.0 Hz, 1H), 5.30 – 5.17 (m, 2H), 5.05 (d, J = 10.0 Hz, 1H), 4.69 (ddd, J = 10.3, 7.7, 2.5 Hz, 1H), 4.57 (d, J = 10.7 Hz, 1H), 4.45 (d, J = 10.6 Hz, 1H), 4.23 (dd, J = 10.5, 1.8 Hz, 1H), 3.79 (s, 3H), 3.43 (t, J = 4.4 Hz, 1H), 3.28 – 3.20 (m, 1H), 3.19 (s, 1H), 2.81 (ddd, J = 10.3, 6.9, 3.9 Hz, 1H), 2.61 (dp, J = 9.3, 6.6 Hz, 1H), 2.54 – 2.42 (m, 3H), 2.19 – 1.93 (m, 3H), 1.89 – 1.75 (m, 2H), 1.75 – 1.58 (m, 4H), 1.58 – 1.52 (m, 4H), 1.05 (d, J = 6.9 Hz, 3H), 1.02 – 0.98 (m, 4H), 0.98 – 0.84 (m, 40H), 0.73 (d, J = 6.7 Hz, 3H), 0.11 – 0.06 (m, 9H);

¹³C NMR: (126 MHz, CDCl₃) δ 170.34, 157.95, 131.98, 131.88, 131.55, 130.91, 130.41, 130.22, 130.19, 130.04, 128.09, 127.98, 112.67, 112.64, 83.80, 83.63, 81.87, 79.33, 76.34, 76.25, 76.00, 75.75, 73.77, 68.35, 63.78, 54.25, 38.90, 37.38, 36.61, 35.09, 34.62, 34.34, 34.15, 33.89, 33.83, 30.57, 28.69, 26.61, 25.50, 25.29, 25.19, 24.84, 24.64, 22.08, 21.98, 19.95, 18.94, 17.91, 17.81, 17.60, 17.37, 17.09, 15.85, 15.34, 13.63, 13.46, 13.32, 12.99, 9.79, 9.63, -4.23, -4.30, -4.33, -4.38, -4.59, -5.22, -5.37, -5.90.

IR (V_{\max} , cm^{-1}): 2958, 2930, 2856, 1745, 1462, 1250, 1083, 835, 775;

$[\alpha]_D^{23}$ + 23.8 (c 1.3 in CH₂Cl₂);

HRMS (ESI) calcd. For C₅₈H₁₀₆O₇Si₃ m/z 998.7246, found 998.7240.



Olefin **F3** (**Figure 1, F3**): The entitled compound was prepared from **F3** using the general procedure and was purified by column chromatography (EtOAc:Hexanes = 0:100 -> 5:95) as a clear oil (55%).

¹H NMR:(500 MHz, Chloroform-d) δ 7.34 – 7.20 (m, 4H), 6.87 (td, J = 5.9, 2.3 Hz, 2H), 5.32 – 5.15 (m, 2H), 5.08 (d, J = 9.9 Hz, 1H), 4.69 (ddd, J = 10.5, 7.8, 2.6 Hz, 1H), 4.52 (d, J = 10.7 Hz, 1H), 4.45 (d, J = 10.7 Hz, 1H), 4.23 (dd, J = 10.4, 2.0 Hz, 1H), 3.80 (s, 3H), 3.47

(t, J = 4.4 Hz, 1H), 3.26 (t, J = 5.2 Hz, 1H), 3.14 (t, J = 5.3 Hz, 1H), 2.62 (dt, J = 9.4, 6.3 Hz, 1H), 2.57 – 2.42 (m, 3H), 2.17 (t, J = 12.3 Hz, 1H), 1.94 (p, J = 6.2 Hz, 1H), 1.91 – 1.79 (m, 1H), 1.79 – 1.67 (m, 3H), 1.65 – 1.46 (m, 8H), 1.45 – 1.08 (m, 8H), 1.02 – 0.80 (m, 48H), 0.74 (d, J = 6.6 Hz, 3H), 0.07 (d, J = 2.7 Hz, 8H), 0.06 (s, 9H);

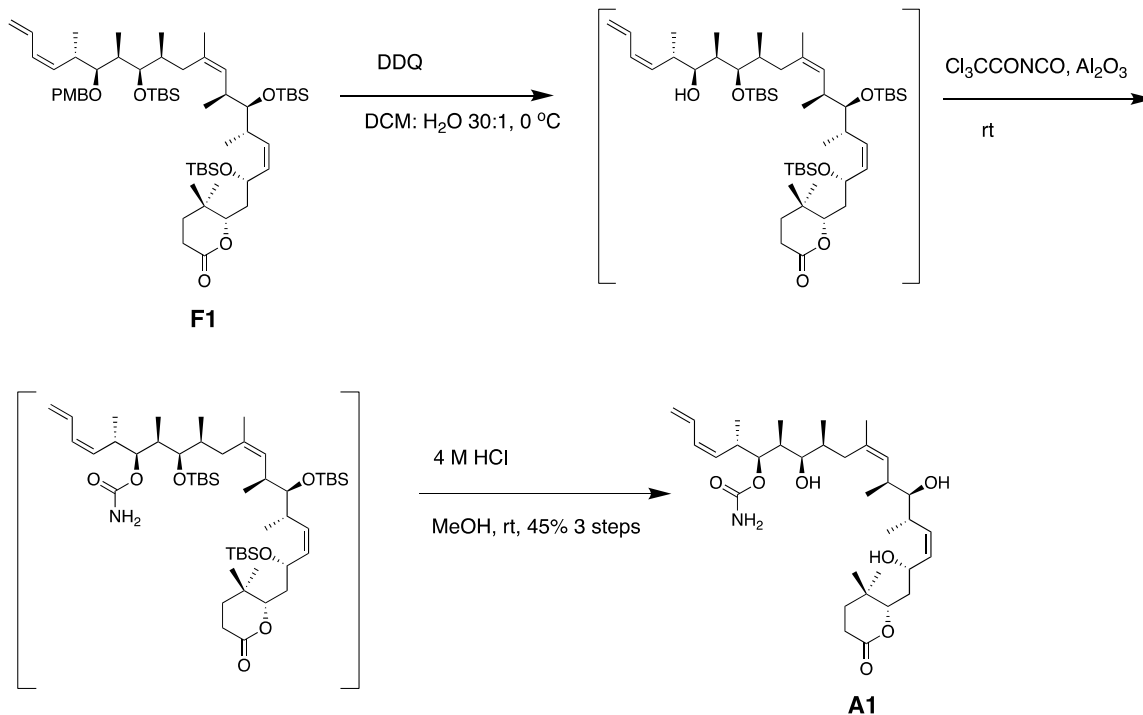
¹³C NMR: (126 MHz, CDCl₃) δ 170.39, 157.98, 132.00, 131.90, 131.05, 130.38, 130.14, 129.62, 128.03, 112.69, 84.49, 81.89, 79.33, 76.56, 76.25, 76.00, 75.75, 73.60, 68.35, 63.78, 54.27, 37.83, 37.37, 36.56, 35.55, 34.78, 34.30, 34.12, 33.88, 33.65, 30.58, 30.57, 29.87, 28.84, 28.70, 28.05, 26.61, 25.90, 25.51, 25.27, 25.20, 24.83, 24.27, 22.09, 22.06, 21.65, 19.69, 18.93, 17.54, 17.38, 17.10, 16.23, 15.92, 15.25, 13.21, 13.12, 12.85, 10.43, 10.24, -4.29, -4.34, -4.36, -5.22, -5.36, -5.90;

IR (V_{max}, CM⁻¹): 2956, 2929, 2856, 1745, 1462, 1250, 1084, 835, 775;

[α]_D²³ + 10.75 (c 0.69 in CH₂Cl₂);

HRMS (ESI) calcd. For C₅₈H₁₀₈O₇Si₃, m/z 1000.7403, found 1000.7400.

General Procedure for the Preparation of Disco-analogs.

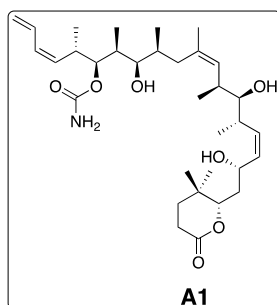


To a 25 ML of round-bottomed flask containing **F1** (115 mg, 0.115 mmol, 1 equiv.) and a magnetic stirring bar, DCM 9ML and DI water 0.3 ML were added sequentially. The mixture was stirred at 0 oC by standing in an ice bath for 10 minutes. At this stage, DDQ (39.2 mg, 0.173 mmol, 1.5 equiv.) was added portionwise. The reaction turned dark green then bloody red. After the addition of DDQ, the reaction mixture was stirred at 0 oC for 2 hours before it was quenched by the addition of sat. NaHCO₃ 5 ML. After separation, the aqueous layer was extracted with EtOAc 3 x 15 ML. The combined organic layers were washed sequentially with DI water 10 ML and sat. NaCl 10 ML and dried over MgSO₄. After the removal of MgSO₄, the filtrate was concentrated and dissolved in 10 ML of premixed EtOAc and hexanes (v:v=20:80). The resulting orange solution was allowed to pass through a short silica gel pad (2 CM x 4 CM) to remove the colored stuff. The filtrate was concentrated and azeotroped with benzene 3 x 2 ML and used directly in the next step without further purification.

The a 10 ML of round-bottomed flask containing the crude alcohol product (78 mg, 0.0894 mmol, 1 equiv.) and a magnetic stirring bar, 2 ML dry DCM was introduced followed by the addition of trichloroacetyl isocyanates (33.7 mg, 0.022 ML, 0.179 mmol, 2 equiv.). The reaction mixture was stirred at room temperature for 30 minutes and then loaded by pipette to a pre-wetted neutral Al₂O₃ pad (1.5 CM x 6 CM) at room

temperature. 4 hours later, the carbamate product was washed off using EtOAc 40 ML and concentrated on rotavapor.

The crude carbamate product was dissolved in methanol 3 ML. To the resulting solution, 1.0 ML of 4N HCl was introduced slowly. The reaction mixture was stirred at room temperature for 4 hours then another 1.0 ML of 4N HCl was added. The reaction was continued to stir at room temperature for another 8 hours then diluted with 100 ML of EtOAc. After separation, the organic layer was washed with DI water till pH value ~ 7.0 and then dried over MgSO_4 . The entitled product was purified by chromatography column.



Analog **A1** (**Figure 1, A1**): The entitled compound was prepared from **F1** using the general procedure and was purified by column chromatography (EtOAc:Hexanes = 40:100 \rightarrow 80:20) as a grey solid azeotroped with benzene and dried under high vacuum (45% over 3 steps).

$R_f = 0.3$ (EtOAc), stained with Cerium Ammonium Molybdate.

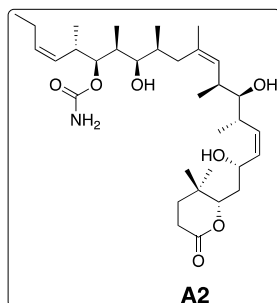
^1H NMR: (500 MHz, Chloroform- d) δ 6.55 (dt, $J = 16.8, 10.6$ Hz, 1H), 5.97 (t, $J = 11.0$ Hz, 1H), 5.45 (dd, $J = 11.2, 7.6$ Hz, 1H), 5.32 (dt, $J = 27.9, 10.5$ Hz, 2H), 5.20 – 4.99 (m, 3H), 4.65 (dd, $J = 7.3, 4.7$ Hz, 2H), 4.55 (s, 2H), 4.29 (dd, $J = 7.6, 5.0$ Hz, 1H), 3.22 (t, $J = 5.1$ Hz, 1H), 3.13 (dd, $J = 7.0, 4.5$ Hz, 1H), 2.94 (dt, $J = 10.1, 6.8$ Hz, 1H), 2.76 (dt, $J = 9.9, 6.8$ Hz, 1H), 2.59 – 2.38 (m, 3H), 1.92 – 1.76 (m, 5H), 1.69 (dt, $J = 13.8, 8.5$ Hz, 1H), 1.64 – 1.52 (m, 7H), 0.98 – 0.84 (m, 20H), 0.77 (d, $J = 5.7$ Hz, 3H);

^{13}C NMR: (126 MHz, CDCl_3) δ 171.72, 157.03, 134.41, 133.61, 133.39, 132.97, 132.10, 132.03, 129.86, 129.68, 128.52, 128.42, 128.30, 117.90, 83.46, 78.92, 78.76, 77.24, 76.99, 76.74, 75.67, 64.47, 37.39, 37.27, 36.01, 35.83, 35.15, 34.73, 34.44, 33.02, 31.58, 29.67, 27.42, 26.36, 23.24, 19.65, 18.36, 17.44, 15.38, 13.80, 8.91, 0.99;

IR (V_{max} , CM^{-1}): 3417, 2965, 2932, 2874, 1713, 1600, 1377, 1045, 732;

$[\alpha]_D^{23}$ + 9.66 (c 0.6 in CH_2Cl_2);

HRMS (ESI) calcd. For $\text{C}_{33}\text{H}_{55}\text{NO}_7$ m/z 577.3979, found 577.3980.



Analog **A2** (**Figure 1, A2**): The entitled compound was prepared from **F2** using the general procedure and was purified by column chromatography (EtOAc:Hexanes = 40:100 -> 80:20) as a grey solid azeotroped with benzene and dried under high vacuum (45% over 3 steps).

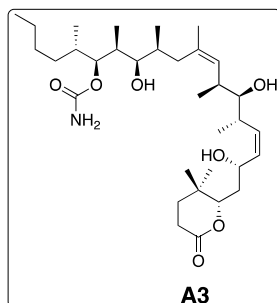
¹H NMR: (500 MHz, Chloroform-d) δ 5.49 (dd, J = 11.1, 7.7 Hz, 1H), 5.44 – 5.34 (m, 2H), 5.30 – 5.21 (m, 1H), 5.16 (d, J = 9.9 Hz, 1H), 4.80 (d, J = 2.8 Hz, 2H), 4.68 (dq, J = 8.4, 4.8, 4.0 Hz, 2H), 4.39 – 4.29 (m, 1H), 3.29 – 3.21 (m, 1H), 3.18 (dd, J = 6.8, 4.6 Hz, 1H), 2.80 (dtq, J = 13.9, 7.0, 4.9, 3.4 Hz, 2H), 2.62 – 2.45 (m, 3H), 2.04 (dddd, J = 20.1, 14.6, 7.2, 1.6 Hz, 3H), 1.89 (tdd, J = 13.9, 9.0, 4.0 Hz, 3H), 1.74 (dt, J = 13.7, 8.5 Hz, 1H), 1.69 – 1.56 (m, 5H), 0.99 (t, J = 3.4 Hz, 5H), 0.97 (s, 1H), 0.96 – 0.91 (m, 11H), 0.82 (d, J = 5.8 Hz, 3H);

¹³C NMR: (126 MHz, CDCl₃) δ 170.87, 156.37, 133.28, 132.17, 131.95, 131.22, 129.22, 128.78, 127.27, 82.48, 78.03, 77.88, 76.25, 76.00, 75.75, 74.89, 63.26, 36.41, 36.31, 35.06, 34.79, 34.06, 33.39, 33.13, 32.13, 30.55, 26.38, 25.31, 22.23, 19.71, 18.64, 17.19, 16.79, 14.33, 13.43, 13.01, 7.83;

IR (V_{\max} , cm^{-1}): 3417, 2965, 2932, 2874, 2247, 1713, 1600, 1458, 1327, 1045, 732;

$[\alpha]_D^{23}$ + 6.27 (c 0.75 in CH₂Cl₂);

HRMS (ESI) calcd. For C₃₃H₅₇NO₇ m/z 579.4135, found 579.4140.



Analog **A3** (**Figure 1, A3**): The entitled compound was prepared from **F3** using the general procedure and was purified by column chromatography (EtOAc:Hexanes = 40:100 -> 80:20) as a grey solid when azeotroped with benzene and dried under high vacuum (50% over 3 steps).

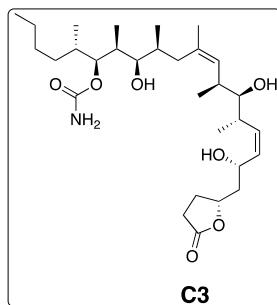
¹H NMR: (500 MHz, Chloroform-d) δ 5.50 (dd, J = 11.2, 7.6 Hz, 1H), 5.41 (t, J = 10.5 Hz, 1H), 5.19 (d, J = 9.8 Hz, 1H), 4.78 (s, 2H), 4.73 – 4.63 (m, 1H), 4.59 (dd, J = 7.8, 3.3 Hz, 1H), 4.35 (dd, J = 7.5, 5.1 Hz, 1H), 3.28 (d, J = 4.8 Hz, 1H), 3.21 (dd, J = 7.1, 4.4 Hz, 1H), 2.83 (dt, J = 9.9, 6.7 Hz, 1H), 2.68 – 2.46 (m, 3H), 2.09 – 1.84 (m, 5H), 1.82 – 1.54 (m, 9H), 1.46 – 1.19 (m, 8H), 1.04 – 0.97 (m, 5H), 0.97 – 0.91 (m, 8H), 0.89 (dq, J = 7.2, 4.0, 3.0 Hz, 7H), 0.83 (d, J = 5.4 Hz, 3H);

¹³C NMR:(126 MHz, CDCl₃) δ 170.80, 156.56, 133.46, 132.46, 131.93, 128.73, 127.31, 82.50, 79.03, 77.93, 76.25, 76.00, 75.75, 75.45, 63.52, 36.43, 36.06, 35.18, 35.05, 34.57, 34.19, 33.44, 32.04, 30.61, 30.33, 28.67, 28.19, 26.81, 26.42, 25.35, 22.32, 21.91, 18.70, 17.30, 14.83, 14.36, 13.07, 12.64, 12.60, 7.76.

IR (V_{\max} , CM^{-1}): 3418, 2963, 2929, 1714, 1459, 1378, 1044, 737;

$[\alpha]_D^{23}$ - 8.94 (c 0.35 in CH₂Cl₂);

HRMS (ESI) calcd. For C₃₃H₅₉NO₇ m/z 581.4292, found 581.4290



Analog **C3** (**Figure 1, C3**): The entitled compound was prepared from **F3** using the general procedure and was purified by column chromatography (EtOAc:Hexanes = 40:60 -> 80:20) as a grey solid when azeotroped with benzene and dried under high vacuum (46% over 3 steps).

¹H NMR: (500 MHz, Chloroform-d) δ 5.54 – 5.44 (m, 2H), 5.16 (d, J = 9.8 Hz, 1H), 4.77 (tdd, J = 8.5, 6.5, 4.2 Hz, 1H), 4.69 (dt, J = 13.4, 6.7 Hz, 1H), 4.62 (qd, J = 8.8, 8.3, 3.5 Hz, 1H), 3.26 (t, J = 5.1 Hz, 1H), 3.20 (dd, J = 6.7, 4.8 Hz, 1H), 2.80 (ddp, J = 13.6, 9.4, 6.8 Hz, 2H), 2.59 (ddd, J = 8.5, 6.9, 4.5 Hz, 1H), 2.57 – 2.51 (m, 1H), 2.38 (dq, J = 13.2, 6.6 Hz,

1H), 2.12 – 1.77 (m, 9H), 1.02 (d, J = 6.7 Hz, 2H), 1.00 – 0.93 (m, 9H), 0.83 (d, J = 6.0 Hz, 3H);

¹³C NMR: (126 MHz, CDCl₃) δ 176.11, 132.69, 131.60, 131.29, 129.35, 128.46, 77.90, 77.87, 76.95, 76.25, 76.20, 76.00, 75.75, 74.90, 64.37, 42.18, 36.37, 34.93, 34.80, 34.16, 33.17, 32.04, 27.83, 27.46, 22.29, 19.75, 17.35, 16.76, 14.53, 13.46, 13.18, 12.84, 7.90;

IR (V_{max}, CM⁻¹): 3418, 3420, 2973, 2970, 2943, 1716, 1460, 737;

[α]_D²³ - 12.20 (c 0.3 in CH₂Cl₂);

HRMS (ESI) calcd. For C₃₀H₅₃NO₇ m/z 539.3822, found 539.3820.

Synthesis of discodermolide analogs **B1**, **B2**, **B3** and **C1** were previously reported by the Smith group.⁴

Synthesis of discodermolide analog **C2** was reported by Kosan Biosciences Inc.⁵

Part 2 - Crystallization of B2, Data Collection and Determination of Structure.

Crystals of T₂R-TTL were generated as described.⁶⁻⁷ Suitable T₂R-TTL crystals were soaked in reservoir solutions containing 5 mM of congener B2 and subsequently flash cooled in liquid nitrogen following a brief transfer into cryo solutions containing 16% and 20% glycerol. T₂R-TTL-B2 data were collected at beamline X06DA at the Swiss Light Source (Paul Scherrer Institut, Villigen, Switzerland). Images were indexed and processed using XDS.⁸ Structure solution using the difference Fourier method and refinement were performed using PHENIX.⁹ Model building was carried out iteratively using the Coot software.¹⁰

Data collection and refinement statistics for T₂R-TTL-B2 are provided in Supplemental Table S6. The resolution cut-off was selected based on the CChalf criterion according to Karplus and Diederichs.¹¹ Molecular graphics and analyses were performed with PyMol (The PyMOL Molecular Graphics System, Version 1.8.6.2. Schrödinger, LLC).

Part 3 - Evaluation of Senolytic Activity in Senescence Cancer Cells.

Cancer cells were made senescent by exposure to Cisplatin (CDDP) or Taxol for 14 days, as previously described.¹² To test the ability of novel congeners to kill senescent tumor cells, (termed senolytic activity), cultures were washed 2x to remove cellular debris and thereafter, treated with DDM or congeners, or panabinostat, a HDAC inhibitor previously demonstrated to have senolytic activity.¹² After 3 days incubation, cell viability was assessed by MTS (Promega) and mean OD \pm SD expressed relative to vehicle-only treatment. Experiments were repeated a minimum of 3x.

References

- 1) Amos B. Smith, Thomas J. Beauchamp, Matthew J. LaMarche, Michael D. Kaufman, Yuping Qiu, Hirokazu Arimoto, David R. Jones, and Kaoru Kobayashi. *J. Am. Chem. Soc.*, **2000**, 122 (36), pp 8654–8664.
- 2) Ian Paterson, Gordon J. Florence, Kai, Gerlach, Jeremy P. Scott, and Natascha Sereinig. *J. Am. Chem. Soc.*, **2001**, 123 (39), pp 9535–9544.
- 3) Amos B. Smith, Scott Freeze, Ming Xian, and Tomoyasu Hirose. *Org. Lett.*, **2005**, 7 (9), pp 1825–1828.
- 4) Amos B. Smith, and Ming Xian. *Org. Lett.*, **2005**, 7 (23), pp 5229–5232; Simon J. Shaw, Kurt F. Sundermann, Mark A. Burlingame, David C. Myles, B. Scott Freeze, Ming Xian, Ignacio Brouard, and Amos B. Smith. *J. Am. Chem. Soc.*, **2005**, 127 (18), pp 6532–6533.
- 5) Shaw, Simon J.; Sundermann, Kurt F.; Burlingame, Mark A.; Zhang, Dan; Petryka, Joseph; Myles, David C. *Bioorganic & Medicinal Chemistry Letters* (**2006**), 16(7), 1961-1964.
- 6) Prota, A. E. *et al.* Structural basis of tubulin tyrosination by tubulin tyrosine ligase. *J. Cell Biol.* **200**, 259-270, (2013).
- 7) Prota, A. E. *et al.* Molecular Mechanism of Action of Microtubule-Stabilizing Anticancer Agents. *Science* **339**, 587-590, (2013).
- 8) Kabsch, W. XDS. *Acta Cryst.* **D66**, 125-132, (2010).
- 9) Adams, P. D. *et al.* PHENIX: a comprehensive Python-based system for macromolecular structure solution. *Acta Cryst.* **D66**, 213-221, (2010).
- 10) Emsley, P. & Cowtan, K. Coot: model-building tools for molecular graphics. *Acta Cryst.* **D60**, 2126-2132, (2004).
- 11) P. A. Karplus, K. Diederichs. Linking crystallographic model and data quality. *Science* 336(6084):1030-3, (2012).
- 12) Samaraweera L, Adomako A, Rodriguez-Gabin A and McDaid HM. A Novel Indication for Panobinostat as a Senolytic Drug in NSCLC and HNSCC. *Scientific Reports* 7(1): 1900, (2017).